

Tectonics

RESEARCH ARTICLE

10.1029/2018TC005340

Key Points:

- Geometry of structures imparts a first-order cooling signal to mineral cooling ages
- Thermochronometers can be used to validate or invalidate balanced cross sections
- An active hinterland ramp is a dominant driver of young cooling ages in eastern Bhutan

Supporting Information:

- Supporting Information S1
- Table S1
- Table S2

Correspondence to:

N. McQuarrie,
nmcq@pitt.edu

Citation:

McQuarrie, N., Eizenhöfer, P. R., Long, S. P., Tobgay, T., Ehlers, T. A., Blythe, A., et al (2019). The influence of foreland structures on hinterland cooling: Evaluating the drivers of exhumation in the eastern Bhutan Himalaya. *Tectonics*, 38, 3282–3310. <https://doi.org/10.1029/2018TC005340>

Received 25 SEP 2018

Accepted 30 JUN 2019

Accepted article online 6 JUL 2019

Published online 2 SEP 2019

The Influence of Foreland Structures on Hinterland Cooling: Evaluating the Drivers of Exhumation in the Eastern Bhutan Himalaya

Nadine McQuarrie¹ , Paul R. Eizenhöfer^{1,2} , Sean P. Long³ , Tobgay Tobgay⁴, Todd A. Ehlers² , Ann E. Blythe⁵, Leah E. Morgan⁶, Michelle E. Gilmore¹ , and Gregory M. Dering⁷

¹Department of Geology and Environmental Science, University of Pittsburgh, Pittsburgh, PA, USA, ²Department of Geosciences, University of Tübingen, Tübingen, Germany, ³School of the Environment, Washington State University, Pullman, WA, USA, ⁴Tobgay & Tobgay Consultancy, P.O. Box 548, Thimphu, Bhutan, ⁵Geology Department, Occidental College, Los Angeles, CA, USA, ⁶Denver Federal Center, U.S. Geological Survey, Denver, CO, USA, ⁷Department of Geological Sciences and Engineering, University of Nevada, Reno, Reno, NV, USA

Abstract Understanding, and ideally quantifying, the relative roles of climatic and tectonic processes during orogenic exhumation is critical to resolving the dynamics of mountain building. However, vastly differing opinions regarding proposed drivers often complicate how thermochronometric ages are interpreted, particularly from the hinterland portions of thrust belts. Here we integrate three possible cross-section geometries and kinematics along a transect through the eastern Bhutan Himalaya with a thermal model (Pecube-D) to calculate the resulting thermal field and predict potential ages. We compare predicted ages to a suite of new and published cooling ages. Our results argue for ramp-focused exhumation of the Main Central thrust from 16 to 14 Ma at shortening rates of 40–55 mm/year, followed by slower rates (25 mm/year) during the last 50 km of Main Central thrust displacement and growth of the Lesser Himalayan duplex from 14 to 11 Ma. Emplacement of frontal Lesser Himalayan thrust sheets occurred rapidly (55–70 mm/year) between ~11 and 9 Ma, followed by a decrease in shortening rates to ~10 mm/year during motion on the Main Boundary thrust. Modern shortening rates (17 mm/year) and out-of-sequence motion on the Main Boundary thrust from 0.5 Ma to present reproduce the young cooling ages near the Main Boundary thrust. We show that the dominant control on exhumation patterns in a fold-thrust belt results from the evolution of ramps and emphasize that the geometry and kinematics of structures driving hinterland exhumation need to be evaluated with their linked foreland structures to ensure the viability of the proposed geometry, kinematics, and thus cooling history.

1. Introduction

The topographic evolution of mountain ranges is the product of both structural uplift along faults and folds and the erosional removal of material driven by the increase in relief and variations in precipitation (Barnes et al., 2012; Dahlen, 1990; Horton, 1999; Koons et al., 1989; Whipple, 2009, 2014; Willett, 1999). These tectonic and climatic factors also control the record of rock exhumation in an orogen (e.g., Ehlers & Farley, 2003; Huerta & Rodgers, 2006; Rahn & Grasemann, 1999; Shi & Wang, 1987; Willett & Brandon, 2002). Attempts to understand how climate and tectonics interact to propel exhumation, as well as differing opinions as to which is the dominant driver of exhumation, have spurred multiple debates, particularly in the eastern Himalaya (Adams et al., 2015; Adlakha et al., 2013; Coutand et al., 2014; Duncan et al., 2003; Gilmore et al., 2018; Grujic et al., 2006; Landry et al., 2016; Long et al., 2012; McQuarrie et al., 2014; McQuarrie & Ehlers, 2015). The range of different hypotheses presented to explain the exhumation history of the eastern Himalaya, as well as the diverse methods of quantifying this history, has led to a suite of related questions. How do you interpret thermochronometric cooling ages in the hinterland of contractional orogens? What drives tectonic uplift, is it active surface-breaking structures or active subsurface structures (such as footwall ramps)? Are the cooling ages indicative of a change in erosive conditions driven by a change in climate or change in tectonics?

In contractional orogenic belts such as the Himalaya, the path of rocks toward the surface involves both vertical uplift over ramps and major lateral transport along shallowly dipping flats (Bhattacharyya &

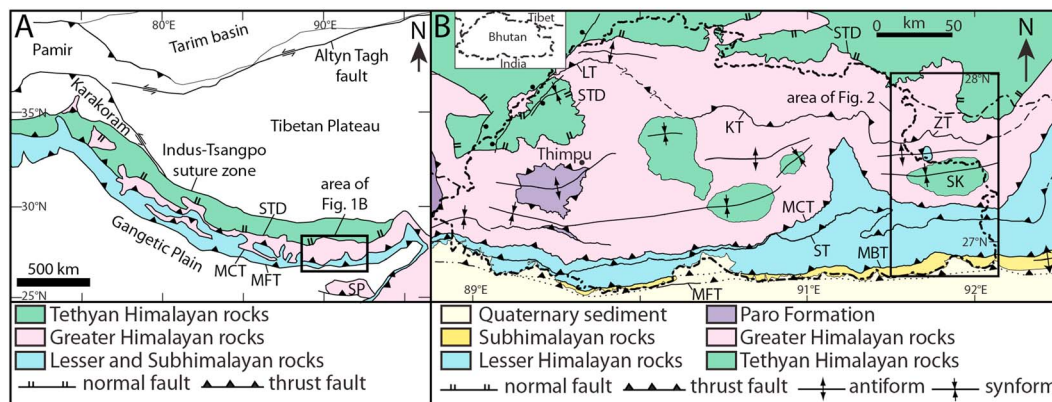


Figure 1. (a) Generalized geologic map of the Himalayan-Tibetan orogen, showing tectonostratigraphic divisions of the Himalayan thrust belt (simplified from Yin, 2006; Long et al., 2017). (b) Simplified geologic map of Bhutan (modified from DeCelles et al., 2016; Long et al., 2017). Structure abbreviations: MFT = Main Frontal thrust, MBT = Main Boundary thrust, ST = Shumar thrust, MCT = Main Central thrust, STD = South Tibetan detachment, KT = Kakhang thrust, LT = Laya thrust, ZT = Zimithang thrust, SP = Shillong Plateau, SK = Sakteng klippe.

Mitra, 2009; Coutand et al., 2014; DeCelles et al., 2001; Gavillot et al., 2018; Long, McQuarrie, Tobgay, & Grujic, 2011, 2012; Robert et al., 2011; Schelling & Arita, 1991; Schelling, 1992; Yin et al., 2010). We contend that the exhumation pattern that results from the evolution of ramps and flats can be exploited to evaluate and then determine the geometry of subsurface structures and critically test potential driving mechanisms for exhumation. The thrusting of rocks up and over footwall ramps concentrates erosional exhumation above these locations and results in young cooling ages. The resulting across-strike pattern of cooling ages describes a broad *U*-shaped curve where cooling ages change from unreset (top of the curve) to young and reset (bottom of the curve), with the youngest ages focused at the top of the footwall ramp. The young, reset ages gently increase in the direction of transport until the tip of the hanging wall ramp, where limited exhumation results again in unreset ages (Lock & Willett, 2008; McQuarrie & Ehlers, 2015; Rak et al., 2017). Multiple ramps complicate the shape of across-strike cooling curves, but in a predictable way (McQuarrie & Ehlers, 2017). Ramps control the amount and location of focused exhumation, and the thermochronometric system that records the resulting signal is dependent on the magnitude of erosion (Gilmore et al., 2018). Therefore, the interaction between subsurface geometry (i.e., the location and magnitude of modern and past ramps) and topographic evolution as reflected in the first-order taper of topography (e.g., Dahlen, 1990) control the across-strike pattern of cooling ages for any given thermochronometric system. These relations allow us to tie hinterland cooling ages to the geometric and kinematic evolution of the fold-thrust belt. We do this by integrating a kinematic model of cross-section deformation that allows for sequential displacement on structures with a thermal model to calculate the resulting thermal field and thermochronometer age. We show how across-strike cooling curves can be used to evaluate the geometry of structures, the locations of ramps, and potentially the rate of faulting. By presenting new mapping in eastern Bhutan (Figures 1 and 2), evaluating several potential cross-section geometries, and integrating a suite of new cooling ages with published cooling ages through the region, we quantify the relationship between structures in the front of the fold-thrust belt and the drivers of uplift and exhumation in the hinterland.

2. Geologic Background

The collision of the Indian and Asian plates at approximately 50–60 Ma (e.g., DeCelles et al., 2014; Klootwijk et al., 1992; Najman et al., 2010; Orme et al., 2016; Patriat & Achache, 1984) initiated thrust faulting and the associated stacking of strata of the northern Indian margin. Metasedimentary and sedimentary rocks deposited on the Indian craton between the early Proterozoic and Paleocene were transported southward by a series of large-offset thrust faults and shear zones (e.g., DeCelles et al., 2002; Gansser, 1964; Mattauer, 1986; Powell & Conaghan, 1973). The resulting Himalayan orogen is divided into tectonostratigraphic zones that are separated by first-order structures (e.g., Burchfiel et al., 1992; Gansser, 1964; Heim & Gansser, 1939). From south to north, these are the Main Frontal thrust (MFT) that places Miocene-Pliocene synorogenic

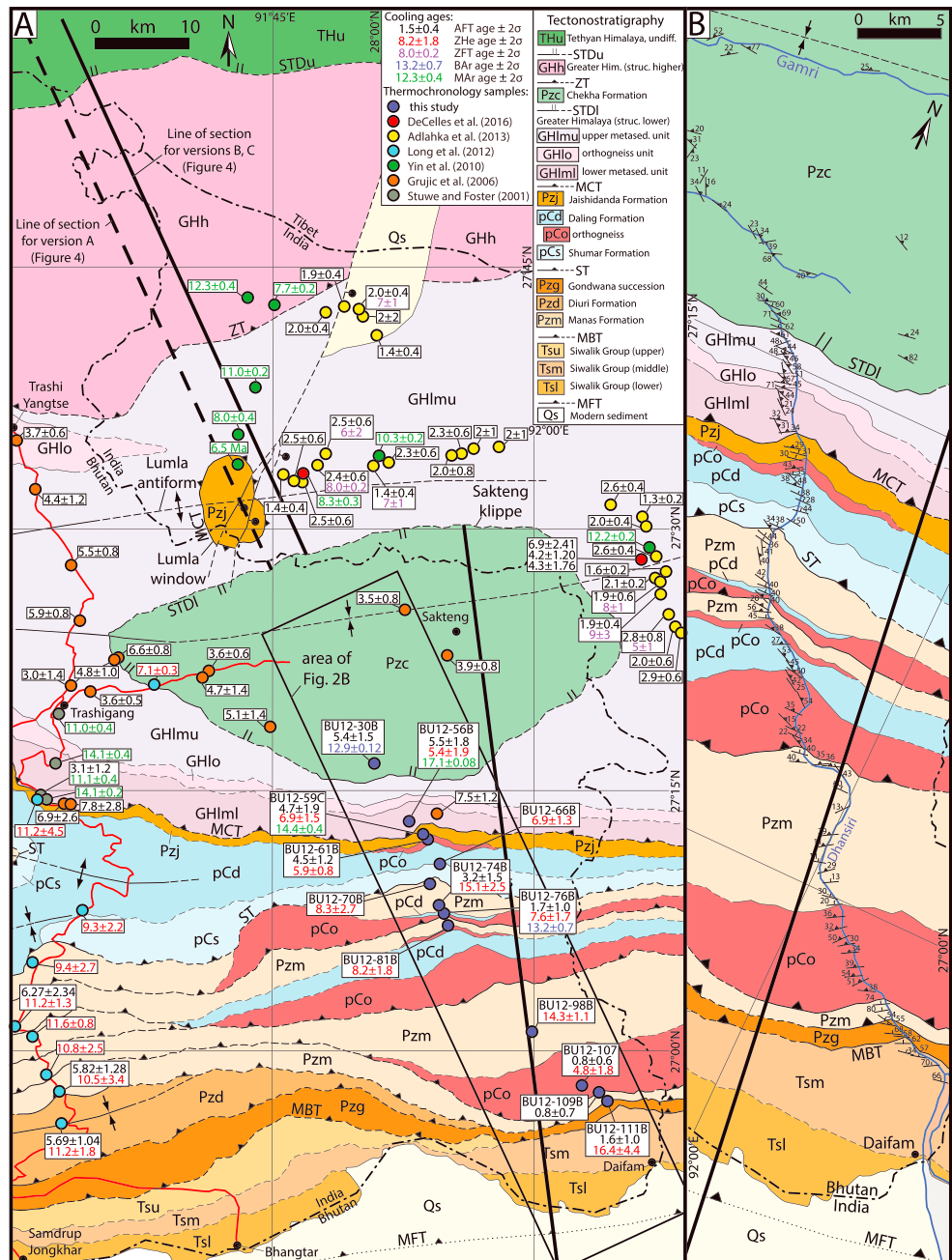


Figure 2. (a) Geologic map of the Dhansiri region in easternmost Bhutan, updated from Long, McQuarrie, Tobgay, Grujic, and Hollister (2011). Stratigraphy, unit abbreviations, structure abbreviations, sources of map data, and symbols are shown in legend. Heavy black line indicates the section line (southern segment is orientated N7°W, northern segment is orientated N23°W), solid red line is road, and solid blue lines are rivers. Black box shows area of Figure 2b. Circles mark locations of thermochronologic data. Dark blue dots indicate new data presented in this study. (b) New detailed mapping along the Dhansiri transect. STDu South Tibetan detachment upper, STDl South Tibetan detachment lower, other structure abbreviations are the same as indicated in Figure 1. AFT = apatite fission track, ZHe = zircon (U-Th)/He, ZFT = zircon fission track, MAR = muscovite $^{40}\text{Ar}/^{39}\text{Ar}$, BAR = biotite $^{40}\text{Ar}/^{39}\text{Ar}$.

sedimentary rocks of the Subhimalayan Siwalik Group over sediments of the modern foreland basin, the Main Boundary thrust (MBT) that places Proterozoic-Paleozoic Lesser Himalayan (LH) rocks over Subhimalayan rocks; the Main Central thrust (MCT), a ductile shear zone that places high-grade Greater Himalayan rocks over LH rocks; and finally, the Southern Tibetan detachment (STD), a top-to-the-north,

normal-sense shear zone that separates Greater Himalayan (GH) rocks from overlying low-grade sedimentary rocks of the Tethyan Himalaya (Figure 1).

2.1. Geologic Mapping

Geologic mapping at a scale of 1:50,000 was focused along the Gamri and Dhansiri Rivers between the towns of Trashigang, Sakteng, and Daifam (Figure 2). Our mapping was integrated with published geologic maps of Bhutan, notably Long, McQuarrie, Tobgay, Grujic, and Hollister (2011) and previously published maps referenced therein (Bhargava, 1995; Gansser, 1983; Gokul, 1983; Grujic et al., 2002; Yin et al., 2010), to connect contacts along strike. Thermochronology samples were collected along the mapped transect.

2.2. Tectonostratigraphy of Easternmost Bhutan

2.2.1. Siwalik Group

A 4-km-thick section of middle Siwalik Group sandstone and conglomerate is exposed along the Dhansiri River north of Daifam (Figure 2). Ridges up to ~1 km in elevation are supported by steeply (~60°) northward dipping, resistant sandstone and conglomerate intervals (Figure 3a). The siltstone- and shale-rich lower Siwalik Group comprises the low-elevation, low-relief landscape between Daifam and the MFT, and is approximately 2 km thick (Figure 2). Coarse, thick-bedded (1–2 m) conglomerate beds are preserved in the immediate footwall of the MBT (Figures 3b and 3c). The entire 6-km-thick section of the Miocene-Pliocene age Siwalik Group (Coutand et al., 2016) has been translated south and uplifted along the MFT.

2.2.2. Gondwana Succession

The MBT carries an ~500-m-thick section of the Permian Gondwana succession (Gansser, 1983; Gokul, 1983; Long, McQuarrie, Tobgay, Rose, et al., 2011), which dips steeply (~55–70°) north (Figure 3b). In this portion of Bhutan, the Gondwana succession consists of organic-rich, friable sandstone, siltstone, and shale with common plant fossils and coal interbeds.

2.2.3. Manas Formation

The southernmost LH thrust fault places ~500 m of the Cambrian Manas formation (Long, McQuarrie, Tobgay, Rose, et al., 2011; McQuarrie et al., 2013) over the Gondwana succession. Along the Daifam-Sakteng transect, the Manas formation is dominated by medium- to coarse-grained quartzite, with interlayered pebble conglomerate layers (Figure 3d) and dark-gray phyllite. Bedding ranges from thin (5–10 cm) and flaggy (Figure 3d) to 0.25–1-m thick, lenticular bedding with trough cross bedding (Figure 4e). The Manas formation lies disconformably over the Paleoproterozoic Daling-Shumar Group (described in section 2.2.5) and associated interlayered orthogneiss bodies (Figure 3f). The upper boundary of the Manas formation is everywhere a thrust fault carrying Paleoproterozoic rocks (Figure 2).

2.2.4. Jaishidanda Formation

The Neoproterozoic-Ordovician Jaishidanda formation (Long, McQuarrie, Tobgay, Rose, et al., 2011; McQuarrie et al., 2013) is dominated by biotite-rich quartzite containing dark lithic clasts that give it a salt-and-pepper appearance (Long, McQuarrie, Tobgay, Grujic, & Hollister, 2011; Long, McQuarrie, Tobgay, Rose, et al., 2011). Interlayers of biotite-garnet schist are also present. Along the Dhansiri River, the Jaishidanda formation is 1 km thick, and like the Manas formation, is also observed in depositional contact above Paleoproterozoic orthogneiss of the Daling-Shumar Group. The upper contact of the Jaishidanda formation is the MCT (Figure 2). The Jaishidanda formation is also exposed in the Lumla window immediately north of the Bhutan-Arunachal Pradesh (India) border (Figure 2; DeCelles et al., 2016; Kesari, 2010; Yin et al., 2010).

2.2.5. Daling-Shumar Group

The Paleoproterozoic Daling-Shumar Group contains two formations: the quartzite-rich Shumar formation is overlain by the schist- and phyllite-dominated Daling formation (Long, McQuarrie, Tobgay, Grujic, & Hollister, 2011; McQuarrie et al., 2008). This section is locally intruded by granite-composition orthogneiss bodies that are up to several kilometers thick. These orthogneiss bodies, both here and in other areas of the Himalaya, are interpreted as Paleoproterozoic granite intrusions that were later sheared and foliated during Himalayan orogenesis (e.g., Kohn et al., 2010). Although orthogneiss bodies are observed at variable stratigraphic levels in the Daling-Shumar Group throughout Bhutan, they are generally thin (100–500 m) and discontinuous (Long, McQuarrie, Tobgay, Grujic, & Hollister, 2011). In western Arunachal Pradesh, the Indian state immediately east of Bhutan, 3–5-km-thick Paleoproterozoic augen orthogneiss bodies are common and are referred to as the Bomdila gneiss (DeCelles et al., 2016). Along our transect in easternmost Bhutan, these



Figure 3. Outcrop photographs of tectonostratigraphic units and formations along the Dhansiri transect. (a) Cliffs of middle Siwalik Group sandstone and conglomerate, white lines highlight bedding. (b) MBT contact between Gondwana succession (right) and Siwalik Group (left); person for scale at MBT. (c) MBT contact with upper Siwalik Group conglomerates; hammer for scale. (d) Thin, planar bedded Manas formation quartzite, scale indicated by white bar. (e) Thick-bedded, channelized Manas formation quartzite, cross bedding highlighted with white lines. Irregular pattern of cross beds in upper bed due to apparent dip and fracture pattern in outcrop. (f) Stratigraphic contact between the Manas formation (thin beds to left) and the Paleoproterozoic augen orthogneiss (more massive and lighter outcrop to right (AG), scale indicated by white bar. (g) Paleoproterozoic augen orthogneiss. (h) Sharp intrusive contact between Paleoproterozoic augen orthogneiss (right) and fine-grained phyllitic quartzite (left) of the Daling formation; pen for scale. (i and j) Outcrop-scale examples of top-to-the-north (i, left; j, right) asymmetric folds. (k and l) Ordovician (McQuarrie et al., 2013) stretched pebble/cobble conglomerate of the Chekha formation, hammer for scale.

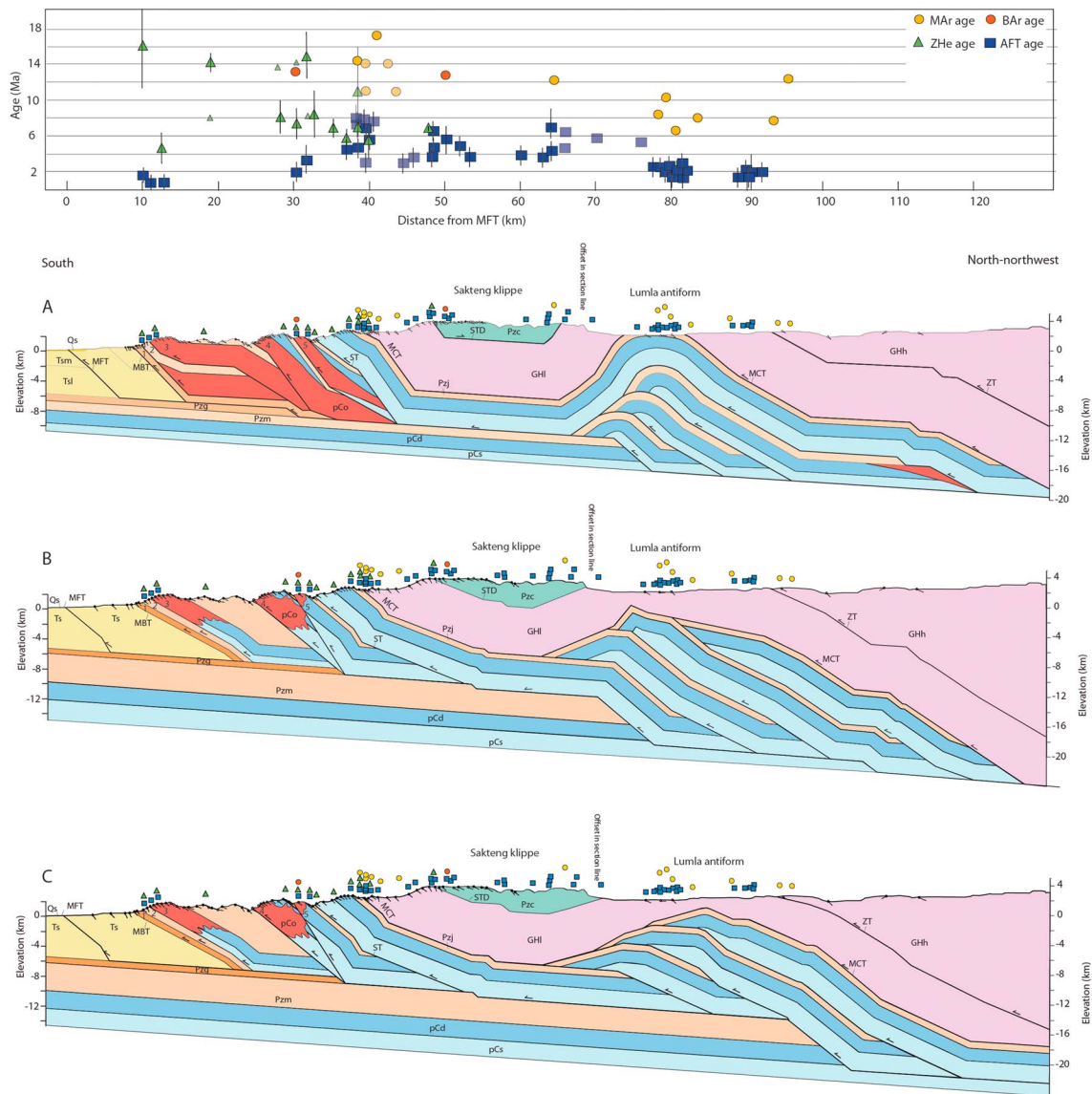


Figure 4. Thermochronologic data (age and location with respect to the trace of the MFT) and balanced cross sections along the Dhansiri transect. Transparent data symbols represent data that are greater than 20 km from the line of section; small ZHe symbols represent single-grain ages not included in the mean age (see Table 1). Line of section and unit abbreviations are shown in Figure 2. ST is Shumar thrust, and ZT is Zimithang thrust. Geometric constraints and differences between the versions A–C are discussed in the text.

orthogneiss bodies are 2–3 km thick and are repeated by four LH thrust faults (Figures 2 and 3). The intrusive contact between the orthogneiss and sedimentary rocks of the Daling formation is well exposed in the fifth LH thrust sheet from the south (Figures 3g and 3h).

2.2.6. Greater Himalayan Rocks

The contact between the LH Jaishidanda formation and GH paragneiss is defined by the upsection appearance of partial melt textures (deformed granitic leucosomes; e.g., Long & McQuarrie, 2010; Long, McQuarrie, Tobgay, Rose, et al., 2011), gneissic banding, and aluminosilicate minerals, which all occur within a narrow (~10 m thick) interval that we map as the MCT. Similar to previous interpretations in Bhutan, we divide GH rocks into a structurally lower level that is exposed above the MCT but below the out-of-sequence Zimithang thrust (ZT), and a structurally higher level that is exposed above the ZT (Figure 2). The ZT, which has been mapped in westernmost Arunachal Pradesh, has been interpreted as the eastern continuation of the Kakthang thrust in Bhutan (DeCelles et al., 2016; Long, McQuarrie, Tobgay, & Grujic, 2011; Yin et al., 2010; Warren et al., 2014). This thrust-sense shear zone is interpreted

to be an out-of-sequence structure that repeats the GH section (Daniel et al., 2003; Grujic et al., 2002; Hollister & Grujic, 2006; Long, McQuarrie, Tobgay, & Grujic, 2011).

The structurally lower GH section has been informally divided into three units, a lower Neoproterozoic metasedimentary unit, a Cambrian-Ordovician orthogneiss unit, and an upper Ordovician age metasedimentary unit (Long, McQuarrie, Tobgay, Grujic, & Hollister, 2011; McQuarrie et al., 2013). In easternmost Bhutan, the lower metasedimentary unit is 3 km thick and is composed of muscovite-biotite-garnet paragneiss with partial melt textures. Kyanite and sillimanite are visible in thin section but are not commonly observed in outcrop. Interbedded quartzite becomes more common upsection. The Cambrian-Ordovician orthogneiss unit, which is rich in feldspar augen, is ~1 km thick. The upper metasedimentary unit is ~2 km thick, and contains paragneiss with partial melt textures near the base, while the higher part of the section is dominated by quartzite- and biotite-rich schist, which commonly contain staurolite.

Similar to the Shemgang region of central Bhutan (Corrie et al., 2012; Long et al., 2017; Long & McQuarrie, 2010), there is no apparent sharp contact between GH rocks and the overlying Tethyan Himalayan section. However, outcrop-scale examples of top-to-the-north shear-sense indicators become increasingly common (Figures 3i and 3j). We place the boundary between GH and Tethyan Himalayan rocks at the southernmost extent of the top-to-north shear-sense indicators, which approximately coincides with the structurally highest occurrence of gneissic banding and partial melt textures. Previous researchers in this region of Bhutan (Chambers et al., 2011; Grujic et al., 2002) have interpreted the GH-Tethyan Himalayan contact as an isolated southern exposure of the South Tibetan detachment (STD) system. Under this interpretation, Tethyan Himalayan rocks above the STD comprise a klippe of rocks (the “Sakteng klippe”) that have been translated northward relative to GH rocks below. We do document the presence of distributed top-to-north shear sense indicators within the GH section; however, mineral assemblages observed through GH and Tethyan rocks do not clearly define a telescoped, upright metamorphic field gradient, as documented across the STD in other parts of the Himalaya (e.g., Cottle et al., 2011; Kellett & Grujic, 2012; Law et al., 2011). After studies in central Bhutan (Corrie et al., 2012; Long et al., 2017), we consider it likely that north vergent shearing may have been diffusely distributed through much of the GH and Tethyan Himalayan sections, in contrast to the discrete STD system documented farther to the north in Tibet.

2.2.7. Tethyan Himalayan Rocks

On the Daifam-Sakteng transect, the Ordovician age Chekha formation (McQuarrie et al., 2013) is the sole Tethyan Himalayan rock unit, and consists of mica-rich, fine- to medium-grained quartzite with both foliation-parallel biotite porphyroblasts and distinct foliation-normal biotite porphyroblasts, similar to the “cross-biotites” described in central Bhutan by Gansser (1983) and Long and McQuarrie (2010). Chekha formation quartzite is medium- to thick-bedded and contains biotite-rich interlayers that often exhibit garnet. Staurolite is common toward the base of the section. Near the base of the Chekha Formation (~500 m above the Tethyan-GH contact) is a conglomerate with clasts that reach 20–40 cm in size (Figures 3k and 3l).

3. Thermochronometry: Methods and Results

We present new muscovite $^{40}\text{Ar}/^{39}\text{Ar}$ (MAr), biotite $^{40}\text{Ar}/^{39}\text{Ar}$ (BAr), zircon (U-Th)/He (ZHe), and apatite fission track (AFT) thermochronometric ages for a suite of samples collected along the transect. Whenever possible, we attempted to obtain three chronometers ($^{40}\text{Ar}/^{39}\text{Ar}$, ZHe, and AFT) from each sample. This was limited by apatite availability as well as only fine-grained neoblastic muscovite in LH metasedimentary rocks. This resulted in three samples that include Ar, ZHe, and AFT ages; four samples with paired AFT and ZHe ages; one sample with a paired AFT and BAr age; and five samples (four ZHe and one AFT), where collection of only one chronometer was possible. The $^{40}\text{Ar}/^{39}\text{Ar}$ analyses were performed at the U.S. Geological Survey Argon Geochronology laboratory in Denver (see Supporting Information S1 for methods). ZHe analyses were performed at the University of Arizona Radiogenic Helium Dating Laboratory (see Supporting Information S2), and AFT data were analyzed at the Occidental College Fission Track Research Laboratory (see Supporting Information S3).

3.1. The $^{40}\text{Ar}/^{39}\text{Ar}$ Ar Data

We obtained MAr ages from one LH Jaishidanda formation sample (BU12-59C) and one GH sample (BU12-56B) ~500 m north of the MCT (Figure 2 and Table 1). Each age is reported with a 2σ error (2 standard

Table 1 (continued)

B.		Published Data									
Longitude	Latitude	Elevation (m)	Map unit	Reference	Age (Ma)	MAE	MAE Error	ZHe	ZHe Error ^a (Ma)	AFT	AFT Error (Ma)
								Mean age (Ma)			
91.527207	27.245589	2480	GH	Sitiwe and Foster (2001)	11.1	0.4				3.1	1.2
91.531034	27.277351	1750	GH	Sitiwe and Foster (2001)	14.1	0.4					
91.546858	27.325629	1060	GH	Sitiwe and Foster (2001)	11	0.4					
91.554472	27.350056	825	GH	Grujic et al. (2006)						3	1.4
91.574528	27.344972	910	GH	Grujic et al. (2006)						3.6	1
91.596833	27.374361	1995	Chekha	Grujic et al. (2006)						4.8	1
91.599833	27.375333	2050	Chekha	Grujic et al. (2006)						6.6	0.8
91.63897	27.35144	1000	Chekha	Long et al. (2012)				7.1	0.3		
91.792417	27.311806	3050	Chekha	Grujic et al. (2006)						5.1	1.4
91.687556	27.362556	1415	Chekha	Grujic et al. (2006)						4.7	1.4
91.687556	27.362556	1415	Chekha	Grujic et al. (2006)						3.6	0.6
91.919389	27.384417	2809	Chekha	Grujic et al. (2006)						3.9	0.8
91.892722	27.415528	2645	Chekha	Grujic et al. (2006)						3.5	0.8
92.1087	27.4563	3024	GH	DeCelles et al. (2016)						6.9	2.41
92.1113	27.4505	2723	GH	DeCelles et al. (2016)						4.2	1.2
92.1156	27.4398	2434	GH	DeCelles et al. (2016)						4.3	1.76
92.113125	27.481276	3736 (from DEM)	GH	Yin et al. (2010)	12.2	0.2					
91.780818	27.545254	2410	GH	Adlakha et al. (2013)						2.5	0.6
91.779867	27.543559	2278	GH	Adlakha et al. (2013)						2.5	0.6
91.921524	27.568979	2557	GH	Adlakha et al. (2013)						2	0.8
91.856067	27.56847	2290	GH	Adlakha et al. (2013)						2.3	0.6
92.725978	27.544297	2356	GH	DeCelles et al. (2016)	8.5	0.3					
91.76311	27.551291	2590	GH	Adlakha et al. (2013)						1.4	0.4
92.167166	27.394415	1663	GH	Adlakha et al. (2013)						2.3	0.6
92.108934	27.502557	4057	GH	Adlakha et al. (2013)						2	1
91.848675	27.558705	2300	GH	Adlakha et al. (2013)						1.4	0.4
91.853429	27.571414	2290	GH	Adlakha et al. (2013)/ Yin et al., 2010	10.3	0.2				2	1
92.108934	27.502557	4057	LH		6.5					2.4	0.6

Table 1 (continued)

Published Data											
	Longitude	Latitude	Elevation (m)	Map unit	Reference	MAr	MAr 2σ	ZHe	ZHe 2σ	AFT	AFT 2σ
						Age (Ma)	Error	Mean age (Ma)	Error ^a (Ma)	Age ^b (Ma)	Error (Ma)
					Adlakhia et al. (2013)/ Yin et al., 2010						
	91.780936	27.543876	2410	GH	Adlakhia et al. (2013)	8	0.4			2.5	0.6
	91.716763	27.591534	2720	GH	Yin et al. (2010)	11	0.2				
	91.7334	27.635995	2527	GH	Yin et al. (2010)						
	91.85224	27.683612	4061	GH	Adlakhia et al. (2013)					1.4	0.4
	91.802328	27.705826	3470	GH	Adlakhia et al. (2013)					2	2
	91.922356	27.570355	2557	GH	Adlakhia et al. (2013)					2	0.4
	92.108934	27.501497	4057	GH	Adlakhia et al. (2013)					2	0.4
	91.821342	27.71323	3550	GH	Adlakhia et al. (2013)					1.9	0.4
	91.751226	27.714287	3472 (from DEM)	GH	Yin et al. (2010)	7.7	0.2				
	91.727458	27.719575	2118 (from DEM)	GH	Yin et al. (2010)	12.3	0.4				

^aZHe error represents both the spread in single grain ages plus the analytical uncertainty. ^bAFT age from this study. Adlakhia et al. (2013) and Grujic et al. (2006) are central FT ages, ages reported by DeCelles et al. (2016) are pooled ages. ^cSingle grain age not included in the reported mean age. See text for discussion.

deviations from the mean; Text S1 and Table S1). BU12-59C yielded an integrated age, interpreted here as a cooling age, of 14.4 ± 0.4 Ma, while sample BU12-56B yielded a plateau age of 17.1 ± 0.06 Ma. Integrated ages represent a weighted mean of all steps on an age spectrum. Plateau ages represent a weighted mean of only congruent plateau steps on an age spectrum. We also analyzed samples from a LH Paleoproterozoic orthogneiss (BU12-76B) and the Chekha formation (BU12-30B) for BAr cooling ages. Samples BU12-76B and BU12-30B yielded BAr ages of 13.2 ± 0.7 Ma (integrated) and 12.9 ± 0.08 Ma (plateau), respectively. Inverse isochron ages for all four samples are either inconclusive (i.e., all steps plot near the $^{36}\text{Ar}/^{40}\text{Ar}$ intercept) and/or consistent with reported integrated and plateau ages. Full analytical details and argon geochronology data are available in Morgan (2019).

3.2. Zircon (U-Th)/He Data

We obtained ZHe ages from 10 LH samples and one GH sample. Each age represents an arithmetic mean of two or three single zircon grains, and is reported with an error that encompasses the range in measured ages and includes a 2σ analytical error. LH samples yielded mean ages that range from 16.4 ± 4.4 to 4.8 ± 1.8 Ma (Table 1 and Figure 2). The GH sample (BU12-56B) produced a cooling age of 5.41 ± 1.89 Ma. The samples from the proximal footwall (Shumar thrust sheet) of the MCT produced ages with a tighter spread that range from 5.4 ± 1.9 to 6.9 ± 1.5 Ma. Samples from LH thrust sheets south of the Shumar thrust (Table 1 and Figure 2) show the greatest variability in age both between samples (16.4 ± 4.4 to 4.8 ± 1.8 Ma), as well as between individual zircon grains (Table 1 and Figure 2). Four samples (BU12-81B, 98B, 74B, and 76B) either had two ages that clustered close to 14.5 Ma with one grain giving an age of ~ 8.5 Ma (BU12-98B, BU12-74B), or two ages that clustered close to 8 Ma (BU12-81B, BU12-76B) with one age at ~ 15 Ma. For these four samples we report the mean of the two grains that are closest in age (Table 1) and plot the sample as a solid triangle in the figures. The remaining age of the third grain is also plotted as a smaller, transparent symbol. The depositional ages of these samples range from 500 to 1,000 Ma (BU12-81B, 98B, and 74B) or 1.8 Ga (BU12-76B; DeCelles et al., 2016; Long, McQuarrie, Tobgay, Rose, et al., 2011; McQuarrie et al., 2013), indicating that the samples in this region were first reset (buried) at ~ 15 – 14 Ma and were close to their closure temperature at ~ 8 – 8.5 Ma with half of the grains cooling through their closure temperature at this time allowing these grains to be reset to the younger age. Different closure temperatures and resulting differences in ZHe dates can be a function of radiation damage (approximated by the effective uranium concentration, eU), grain size, or chemical zonation in the zircon (Guenther et al., 2013, 2014); however, neither variation nor covariation in eU or grain size uniquely explains the two age populations (Text S1 and

Table S2). Sample BU12-107 located ~13 km north of the MFT yielded the youngest ZHe age (4.8 ± 1.8 Ma).

3.3. Apatite Fission Track Data

Nine samples contained sufficient apatite to allow for AFT dating. AFT ages are reported with a 2σ error. The youngest AFT ages range from $0.8 + 0.9/ - 0.4$ to $1.6 + 0.9/ - 0.4$ Ma and are located at the southern limit of the map area, within 3 km of the MBT (BU12-107, 109B, and 111B; Figure 2). The next set of six samples are located ~20 km to the north and range in age from $1.7 + 1.3/ - 0.7$ to $5.5 + 2.0/ - 1.5$ Ma, with ages increasing to the north. AFT ages are reported with a mean error (i.e., ± 1.0 Ma) in Figure 2; however, all of the age-distance plots (e.g., Figure 4 and Table 1) and the resulting interpretations include the full 2σ error for each sample.

3.4. Previously Published Cooling Ages

Recent work in eastern Bhutan and Arunachal Pradesh has produced a wealth of published cooling ages to the west, east, and north of the new data presented in this study. To highlight possible along-strike changes in exhumation as well as to populate the full extent of our cross-section line with measured cooling ages, we have included published MAR, zircon fission track (ZFT), ZHe, and AFT cooling ages in Figure 2. Samples that are located >20 km from the line of section are shown as transparent symbols on age versus distance plots of the data.

Published MAR ages are the youngest (6.5 – 10.3 ± 0.2 Ma) in proximity to the Lumla antiform (DeCelles et al., 2016; Yin et al., 2010) and in the hanging wall of the ZT (7.7 ± 0.2 – 12.3 ± 0.4 Ma; Yin et al., 2010). Other published MAR ages from GH rocks range in age from 11.0 ± 0.4 to 14.1 ± 0.4 Ma (DeCelles et al., 2016; Stüwe & Foster, 2001; Yin et al., 2010), slightly younger to overlapping with the new MAR and BAR ages presented here.

The ZFT ages are from a transect through GH rocks in Arunachal Pradesh that wraps around the eastern and northern edges of the Sakteng klippe. The ages range from 9 ± 3 to 5 ± 1 Ma, and cluster around 7–8 Ma (Adlakha et al., 2013). Previously published ZHe ages from LH rocks were obtained 40 km to the west of our section along the Trashigang transect of Long et al. (2012). These data are weighted mean cooling ages and range in age from 11.6 ± 0.8 to 9.3 ± 2.2 Ma (Figure 2) along a 40-km across-strike distance (Long et al., 2012). The Trashigang ZHe ages all fall between the 7.5 ± 1.7 to 16.4 ± 4.4 ages presented here. The LH Trashigang data are only shown on the map and are not used to evaluate model results.

Over 50 published AFT ages show variable cooling between 7.8 ± 2.8 and 0.8 ± 0.8 Ma (Adlakha et al., 2013; DeCelles et al., 2016; Grujic et al., 2006; Long et al., 2012; Stüwe & Foster, 2001). Figures 2 and 4 highlight that AFT ages generally young to the east and north (between 40 and 90 km north of the MFT) but also display an ~3–4-Ma variability that may not be entirely a function of variable exhumation. Ages from the same study (Grujic et al., 2006) over a restricted structural and geographic area (western edge of Sakteng klippe) demonstrates a range in measured AFT ages that show no age-elevation relationship. Even with this variability, the entire data set shows AFT ages getting younger from the southern trace of the MCT (4–7-Ma ages) to the north (3.7–1.4-Ma ages; Figures 2 and 4).

4. Balanced Cross Sections: Methods and Results

Three different versions of a balanced cross section (versions A, B, and C) were constructed based on the new field data projected onto the section line (Figure 2), to test the sensitivity of cooling ages to variations in cross-section geometry. The line of section is oriented N7°W from Daifam to the northern edge of the Sakteng klippe. This orientation is perpendicular to the trend of major structures and thus parallel to the principal direction of shortening. It is also parallel to mineral stretching lineations measured in LH, GH, and Tethyan Himalayan rocks. North of the Sakteng klippe, the section line is offset ~15 km to the west and trends N23°W, approximately normal to the trace of the ZT and foliations through that region (Yin et al., 2010). The northern segment of the line of section for cross section A is located 4 km west of the line of section shown in Figure 2, in order to intersect the Lumla window (Figures 2 and 4). The cross sections are constrained by surface data (our mapping; Yin et al., 2010), and geophysical data that support an average dip of 4–5°N for the Main Himalayan thrust (Mitra et al., 2005; Ni & Barazangi, 1984; Singer et al., 2017).

Line lengths of the rocks carried in each thrust sheet depicted on the cross sections were matched on the restored sections, specifically ensuring that hanging wall ramps and décollements match footwall ramps and décollements between the deformed and restored sections (e.g., Dahlstrom, 1969; Woodward et al., 1989; Figure S3). Apparent dips were calculated from surface data and projected along-strike to their position on the cross section. Panels of dipping strata were divided into similar dip domains, based on the average apparent dips of surface data. Where different interpretations of dip domains were possible (e.g., for the southernmost three LH thrust sheets), varying cross-section interpretations highlight these differences (Figure 4). No attempt was made to incorporate outcrop-scale folding or to account for penetrative ductile deformation in rocks proximal to the MCT (e.g., Long, McQuarrie, Tobgay, & Hawthorne, 2011, 2016).

One of the largest unknowns in constructing balanced cross sections is the position of hanging wall cutoffs. The hanging wall cutoffs for all of the thrust sheets (except for one small-offset LH sheet) have been eroded. Cross section B (Figure 4b) used conservative geometries that minimize shortening in all cases. The other two geometries (Figures 4a and 4c) require erosional removal of the hanging wall cutoff plus an additional length of the thrust sheet (~10–20 km) in either the MBT sheet, which carries the upper LH Gondwana succession, or the thrust fault immediately north of the MBT that carries a thin section of the LH Manas formation (Figure 2). In these instances, additional fault displacement and erosion were needed to change the location of the footwall ramp at the northern limit of the frontal thrust sheets (Figures 4 and S3). These changes were made to control the location of this large ramp and place it either immediately under the Lumla antiform or immediately north of the youngest cooling ages (Figures 2 and 4).

4.1. Main Frontal Thrust Sheet and Lesser Himalayan Thrust Sheets

All three versions of the cross section show a 5.5-km-thick thrust sheet of the Siwalik Group uplifted above the MFT, which is bound above by a steeply (40–60°) north dipping MBT (Figure 3b). The MBT carries an ~1-km-thick sheet of the Gondwana succession (Figure 4). At the northern limit of the Gondwana succession, a second LH thrust sheet carries a 1-km-thick section of the Manas formation. The cross sections diverge in their depiction of the LH thrust geometry for this thrust sheet and the next thrust sheet to the north (third LH thrust sheet; Figure 4). The differences are a function of two fundamental questions: (1) how to best represent the variation in dips across the Manas formation carried by the third LH thrust? and (2) what is the original thickness of the Manas formation in easternmost Bhutan? Dip angles measured from the Manas formation range from 11 to 60°. The steepest dips are concentrated along the northern limit of the Manas formation (35–60°) in the immediate footwall of the next thrust to the north, while the shallowest dips (11–13°) are concentrated in a 5-km-wide center portion. Cross section A (Figure 4) places significant weight on the 5-km-wide section of shallow dips, and shows a Manas formation thickness that is approximately the same as exposures observed in three other LH thrust sheets north of the MBT. The thin Manas formation section and the shallow dips require a repeated section of orthogneiss and Manas formation at depth. Cross sections B and C assume that the low dips are minor variations and use the average of all of the measured dips (30°), which results in a 4-km-thick Manas formation section overlying the orthogneiss, creating a 6.5-km-thick thrust sheet above the third LH thrust. This requires the second thrust sheet to only carry a thin, 1-km-thick portion of the upper Manas formation (Figure 4). The actual thickness of the Manas formation in easternmost Bhutan is unknown. Where the Manas formation is repeated in a series of thrust faults further to the west, along the road from Trashigang to Samdrup Jongkhar (Figure 2), it is 2.1 km thick (Long, McQuarrie, Tobgay, & Grujic, 2011; McQuarrie et al., 2008). In Arunachal Pradesh, the Rupa Group (correlative to the Baxa Group) ranges in thickness from 2 to 5 km, with a lower siliciclastic section (potentially an along-strike equivalent to the Manas formation) that is ~800 m thick (DeCelles et al., 2016).

The next three LH thrust faults display smaller differences between the cross sections than the first three faults; however, those differences are still a function of how measured dips are portrayed in the subsurface. Cross section A is drawn assuming that the larger percentage of steeper dips (35–56°) in the fourth LH thrust sheet are more representative of the regional dips; thus, the basal thrust is shown with an inflection that allows dips to steepen from 30° in the south to 50° in the north (Figure 4). Cross sections B and C use the average dip (40°) for the entire thrust sheet. These subtle changes in how measured dips are represented in the cross section control the subsurface locations of ramps and flats necessary to best accommodate the interpretation of surface dips.

4.2. Shumar Thrust and MCT

Cross section A also differs from cross sections B and C in the dip of the Shumar thrust sheet and the over-riding MCT (Figure 4). The inflections in displayed dips from shallow dips proximal to the MCT to steeper dips to the north in cross section A is an attempt to match the two extremes in measured data on the southern (shallow) and northern (steeper) extents of exposed GH rocks. Cross sections B and C show a more uniform dipping section of LH and GH rocks based on averaging the measured dips across this section. The result is a very flat base to the syncline of Tethyan Himalayan rocks exposed in the Sakteng klippe in cross section A, in contrast to the modest northward dipping measurements through the region and depicted in cross sections B and C. These sections show an asymmetric syncline with a 30° dipping southern limb and a steeper dipping (~40°) northern limb.

4.3. Lumla Antiform

The most significant difference between all three cross sections is the geometry of the duplex under the Lumla antiform (Figure 4). The presence of a duplex of repeating LH thrust sheets north of the MCT and Sakteng klippe is required by the Lumla window through the MCT, which exposes LH rocks (DeCelles et al., 2016; Kesari, 2010; Yin et al., 2010) and is a component of every published cross section through the region (e.g., DeCelles et al., 2016; Yin et al., 2010). What varies among published sections is the geometry, kinematics, and thus age of duplex formation. Because the growth of the duplex will drive the attainment of structural relief, topographic relief, and exhumation in this region, we show three different permissible geometries that all have different implications for the age and location of exhumation through time. Cross section A was constructed under the assumption that the duplex under the Lumla antiform formed concurrent with the southernmost thrust structures (MFT, MBT, and second LH thrust), requiring that slip accommodated by each fault in the duplex was fed southward onto the MBT and MFT. This geometry argues for young duplex formation, young uplift, and exhumation of the Lumla window and an active ramp under the Lumla antiform (Figure 4a). Cross section B also has the active ramp under the Lumla antiform (Figure 4b). However, this ramp is through the Manas formation and upper portion of the Daling-Shumar Group, and is the footwall ramp of the third LH thrust. In this scenario, the duplex formed significantly earlier in the deformation history, immediately following emplacement of the MCT, but owes its recent structural uplift and associated erosional exhumation to the active ramp through the Manas formation. Although both cross sections A and B have mechanisms to explain the duplex geometry and young exhumation of the Lumla antiform, young (1.4 to 2 Ma) AFT ages extend northward to the immediate footwall of the ZT (Figure 2). Placing the active ramp north of the Lumla antiform in cross section C (Figure 4c) provides a mechanism for driving the young exhumation observed to the north.

4.4. Zimithang Thrust

All three cross sections show the out-of-sequence ZT (DeCelles et al., 2016; Long, McQuarrie, Tobgay, & Grujic, 2011; Warren et al., 2014; Yin et al., 2010). Cross sections A and B present a model where the footwall cutoff for this ductile thrust is at the main detachment level (the Main Himalayan Thrust (MHT)) in the modern cross section. However, the geometry of this branch point from the MHT to the ZT evolves as deformation progresses with time, and the geometry of structures when the fault is active (Figure 5) is not the same geometry as portrayed in the final step. Thus, the geometry in cross section C was designed for the minimum displacement necessary to repeat the entire GH section (Figure 4).

5. Flexural Kinematic Modeling: Methods and Results

5.1. Methods

Cross sections were kinematically and flexurally modeled using *Move* (Midland Valley). Each cross section was deformed in ~10-km increments, which incorporated isostatic loading due to fault displacement and unloading due to erosion. The magnitude of isostatic loading was calculated from the difference between the newly deformed topography and the topography of the previous step (McQuarrie & Ehlers, 2015). Erosional unloading was determined by the difference between the deformed, loaded topography, and a new predicted topographic profile. The new topographic profile assumes a 0-m elevation in the foreland, and an approximate 2° topographic slope from the deformation front toward the hinterland, based on the present topographic angle of this portion of the Bhutan Himalaya (Figure 4). Where structural uplift has

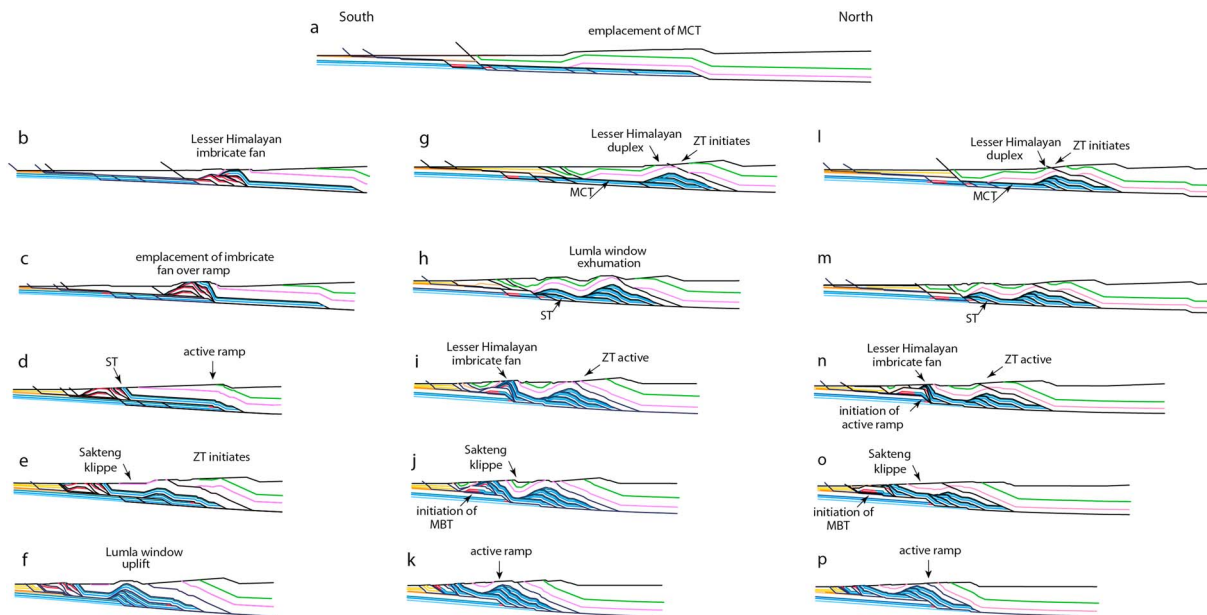


Figure 5. Sequentially restored kinematic scenarios for the three different cross-section geometries shown in Figure 4. (a) Emplacement of the MCT (schematically represented for all three geometries). (b–f) Sequential restoration of cross section A. (g–k) Sequential restoration of cross section B. (l–p) Sequential restoration of cross section C. MBT is Main Boundary thrust, MCT is Main Central thrust, ST is Shumar thrust, and ZT is Zimithang thrust. See text for discussion.

occurred, the topography increases at this prescribed angle. In locations where uplift has not occurred, the new topographic surface simply follows the old topographic surface. Thus, topography is increasing where structural elevation is increasing and staying the same or subsiding where structural elevation is not generated (Gilmore et al., 2018; McQuarrie & Ehlers, 2015). Because the topographic evolution is a function of the cross-section kinematics, that is, how uplift changes in space and time, the final predicted topography provides a first-order test to the viability of the cross-section kinematics.

Flexural-kinematic models are considered viable when the final model can reproduce the observed geology at the surface, the foreland basin thickness (~6 km), and the décollement dip (~4°). Effective elastic thickness, crustal density, and initial décollement dip were systematically varied to optimize the fit of the final modeled cross sections to the original cross sections (Figure 4). In addition to the lines that represent the lithologic units described in section 4, we inserted a 0.5 × 0.5-km grid of unique points and sequentially deformed the grid with 10-km increments of displacement. This deformed grid was used to create a velocity field by assigning a time duration to each step. The time duration between each 10-km increment was varied between different model simulations to evaluate the sensitivity of predicted age to modeled velocity. A constant shortening rate of 17.5 mm/year was evaluated first, and then more complex shortening histories were explored.

5.2. Main Central Thrust: Results

Sequential results from the flexural-kinematic modeling are shown in Figure 5. The emplacement of the MCT over LH rocks is similar for all three models and was modeled as the emplacement of a single thrust sheet over LH rocks. In addition, we did not model top-to-the-north displacement on the STD concurrent with motion on the MCT (Chambers et al., 2011; Grujic et al., 2002). However, as illustrated by the final MCT step before duplex formation (Figure 5a), a top-to-the-north, surface breaking normal fault developed along the GH-Chekha formation contact would have to have accommodated less than 30 km of displacement to prevent removal of the Chekha formation preserved in the Sakteng klippe.

5.3. LH Thrusts and Duplex: Results

In cross section A, the deformation following MCT emplacement builds the imbricate fan in the Daling-Shumar Group and Manas formation represented by LH thrusts 2–6 (Figure 5b). In this scenario, the fault with the greatest amount of displacement is the second LH thrust. It moved 130 km to place orthogneiss

Table 2
Numerical Model Parameters

Property/parameter	Model input value
Material properties	
Crustal volumetric heat production	2.0–4.0 mW/m ³
<i>e</i> -folding depth of crustal heat production	20 km
Thermal conductivity	2.5 W/m K
Specific heat capacity	800 J·kg ⁻¹ ·K ⁻¹
Crustal density	2600 kg/m ³
Mantle density	3300 kg/m ³
Numerical properties	
Temperature at base	1300 °C
Model base	110 km
Surface temperature at 0 km	24°
Atmospheric lapse rate	7°/km
Kinematic grid spacing	0.5 km
Displacement increment	~10 km
Model domain ^a	(650–900) × 110 × 5 km
Horizontal node spacing (numerical model)	1.0 km
Vertical node spacing (numerical model)	1.0 km
Model start time	50 Ma

^aCross section A, 835 km; cross section B, 650 km; cross section C, 650 km.

and the Manas formation over the Gondwana succession (Figures 5b–5d), which positioned the next active ramp north of the future Sakteng klippe (Figure 5e). Thus, in this model, the age, displacement, and exhumation of the frontal thrusts began when the MCT motion ceased. The first period of movement on the ZT occurred after the southward displacement of the imbricate fan in order to rebuild taper (between Figures 5d and 5e). Following initial motion on the ZT, the duplex under the Lumla window grew as displacement was fed south and initiated motion on the MBT. Additional motion on the ZT occurred right before motion on the MFT. Motion on the MFT was accompanied by motion on the last horse of the duplex, driving active uplift and exhumation in the Lumla window (Figure 5f).

In cross section B, the kinematics of deformation are more straightforward and follow a broadly southward propagating pattern of deformation. After initial emplacement of the MCT, the LH duplex formed with the MCT acting as the roof thrust, which facilitates continued motion on the southern portion of the MCT (Figure 5g; Long et al., 2012). Initial growth of the LH duplex is followed by the first phase of displacement on the ZT (following Gilmore et al., 2018). Motion on the Shumar thrust (Figure 5h) and growth of the LH imbricate fan (Figure 5i) created the initial shape of the Sakteng klippe, and was followed by the second pulse of motion on the ZT. Emplacement of orthogneiss and the Manas forma-

tion over the Gondwana succession (Figure 5j) and motion of the MBT and MFT (Figure 5k) moved the active ramp to its final location under the Lumla window.

Cross section C follows almost identical kinematics to cross section B. Key differences are that the full LH duplex formed before initial motion on the ZT (Figure 5l) and that displacement on the MBT and the second LH thrust (Figures 5n and 5o) were greater, which places the active décollement ramp farther to the north (Figure 5p), proximal to the trace of the ZT.

6. Pecube Model: Methods and Results

6.1. Methods

The velocity fields created from the deformed 0.5 × 0.5-km grid of unique points and their assigned ages combined with the final topography for each increment of deformation modeled in Move are input into a University of Tübingen modified version of the thermokinematic model, Pecube-D (Braun, 2003; McQuarrie & Ehlers, 2015; Whipp et al., 2009). Pecube solves the three-dimensional heat transport equation and derives the time-temperature (*t*-*T*) history of particles based on their transport path. The *t*-*T* history of rocks exhumed to the surface is used to calculate thermochronometer ages based on a suite of age prediction algorithms that take into account mineral kinetics and cooling rates (Braun, 2003; Braun et al., 2006; Ehlers et al., 2005). In detail, AFT ages are predicted using the kinetic parameters determined by Crowley et al. (1991). ZHe ages are based on the average zircon kinetics from Reiners et al. (2004). MAr ages are calculated based on the concepts of Dodson (1973) as implemented by Robbins (1972), Hames and Bowring (1994), and Braun et al. (2006).

The model domain is 650–850 km long, depending on the cross-section model, and 110 km deep. Constant-temperature boundary conditions were applied to the base (1,300 °C) and surface (24 °C and 0-m elevation). The surface temperature was decreased with elevation at an atmospheric lapse rate of 7 °C/km. A range of material properties was explored in model simulations. The thermal state of the crust depends on the basal heat flow from the mantle and the material properties of the crust (e.g., thermal conductivity, density, heat capacity, and radiogenic heat production). We prescribe an exponential decrease in heat production with depth, as opposed to assuming a constant crustal heat production. An exponential decrease in heat production with depth requires definition of surface heat production (A_0) and an *e*-folding depth (McQuarrie & Ehlers, 2017). All model parameters are summarized in Table 2.

6.2. Effect of Geometry: Results

We evaluate the effect of changing cross-section geometry on cooling ages by examining the predicted cooling ages from all three geometries using a constant velocity (17.5 mm/year) and a surface heat production value of $3.0 \mu\text{W}/\text{m}^3$.

For cross section A, the MCT is active from 19 to 13 Ma. The associated cooling with this motion produces reset MAr ages that are oldest (~18 Ma) in the Sakteng klippe, and get progressively younger to the north. After MCT motion, initial deformation of the LH imbricate fan (second through fifth LH thrusts) occurs from 13 to 10 Ma (Figures 4 and 5b), assuming a constant velocity of 17.5 mm/year. Following this initial formation, these structures are translated southward over the footwall ramp of the frontal LH thrust sheet (Figure 5c), driving uplift and exhumation of the imbricate fan between 10 and 8 Ma. Predicted ZHe ages of 9–9.5 Ma between 20 and 40 km north of the MFT and ages that increase from 10 to 14 Ma between 40 and 55 km north of the MFT directly reflect the exhumation associated with the southward younging imbricate fan, and uplift-induced exhumation as it was lifted over the ramp from 10 to 9 Ma (Figure 6). The broadly predicted AFT ages of 8 Ma across this same 35-km distance reflect continued exhumation as the thrust sheets were displaced along a flat (Figures 5c and 5d) and exhumation of the Sakteng klippe over the ramp. The growth of the LH duplex from 3.5 to 2 and 0.5–0 Ma is reflected in the predicted AFT cooling ages of 2 Ma located 80–90 km north of the MFT (Figure 6). Duplex formation was concurrent with displacement on the MBT, which produced the 2-Ma AFT ages above the MBT ramp. Predicted ZHe ages ~80–90 km north of the MFT are ~6 Ma (the age that these rocks were translated over the LH ramp shown in Figure 5d) and younger, indicating additional cooling and younging of these ages due to duplex formation. Predicted ZHe and AFT ages north of the ZT (100–120 km) are between 4 and 2 Ma (Figure 6) and reflect the two pulses of ZT cooling from 4 to 3.5 and 2 to 0.5 Ma, assuming a shortening rate of 17.5 mm/year. The geometry and kinematics of cross section A reproduce the young AFT ages between 75 and 95 km north of the MFT, but do not reproduce the MAr ages from the same region that range from 6.5 to 12.3 Ma (Figure 6). The 14–10-Ma period of cooling as the imbricate fan formed is reflected in the modeled ZHe ages, consistent with 3 of the 11 measured ZHe ages. However, the final pulse of young exhumation associated with the MBT and MFT was not sufficient to match the southernmost AFT and ZHe cooling ages between 10 and 15 km north of the MFT. The largest mismatch is the difference between the predicted AFT ages of 8 Ma and the measured AFT ages that range from 6 to 2 Ma between 30 and 65 km north of the MFT. Windows of time with velocities faster than 17.5 mm/year, such as a rate of 60 mm/year between 5 and 2.5 Ma, will produce AFT ages as young as the measured ages between 10 and 60 km north of the MFT; however, such fast rates would produce very young ZHe ages (~4.5 Ma), significantly younger than the ~8-Ma measured ZHe ages between 25 and 40 km north of the MFT.

In contrast to the older predicted AFT and ZHe ages produced by cross section A, cross section B produced predicted AFT and ZHe ages younger than 4 Ma between 12 and 50 km north of the MFT. The young predicted AFT ages continue until immediately north of the active ramp located at 80 km north of the MFT, matching the young measured ages in the region of the Lumla antiform. The 1–2-Ma AFT ages predicted to the south only match the youngest three samples between 30 and 70 km north of the MFT, and the predicted ages above the MBT are limited in their southern extent and only match one of the three young AFT ages located ~10 km north of the MFT. At a constant velocity of 17.5 mm/year and an A_0 value of $3.0 \mu\text{W}/\text{m}^3$, the geometry for cross section B produces reset MAr ages that match the measured ZHe ages in the region between 25 and 35 km north of the MFT (Figure 6). In the region of the Lumla antiform, the predicted ZHe and MAr ages produce the southward younging signal expected for a hinterland dipping duplex (Lock & Willett, 2008; McQuarrie & Ehlers, 2017). Assuming constant rates of 17.5 mm/year, the duplex formed between 14.4 and 8 Ma. While a broadly southward younging signal is apparent in the measured MAr ages, consistent with the geometry of a hinterland dipping duplex, the predicted ages of 13–17 Ma are 5–6 Myr older than the 6.5–12.3-Ma measured ages. Predicted ZHe ages overlap with measured MAr ages between 80 and 100 km north of the MFT, highlighting that while the pattern of cooling in the predicted ages is similar to the measured ages, additional exhumation that is significantly younger is needed to predict MAr ages that are as young as the measured ages. Because the duplex forms early in this geometry, there is no structural mechanism to drive the young exhumation. In this model, the ZT is active from 9.5 to 10.5 Ma and then again from 4 to 5 Ma. The predicted ZHe and AFT ages record this younger period of activity.

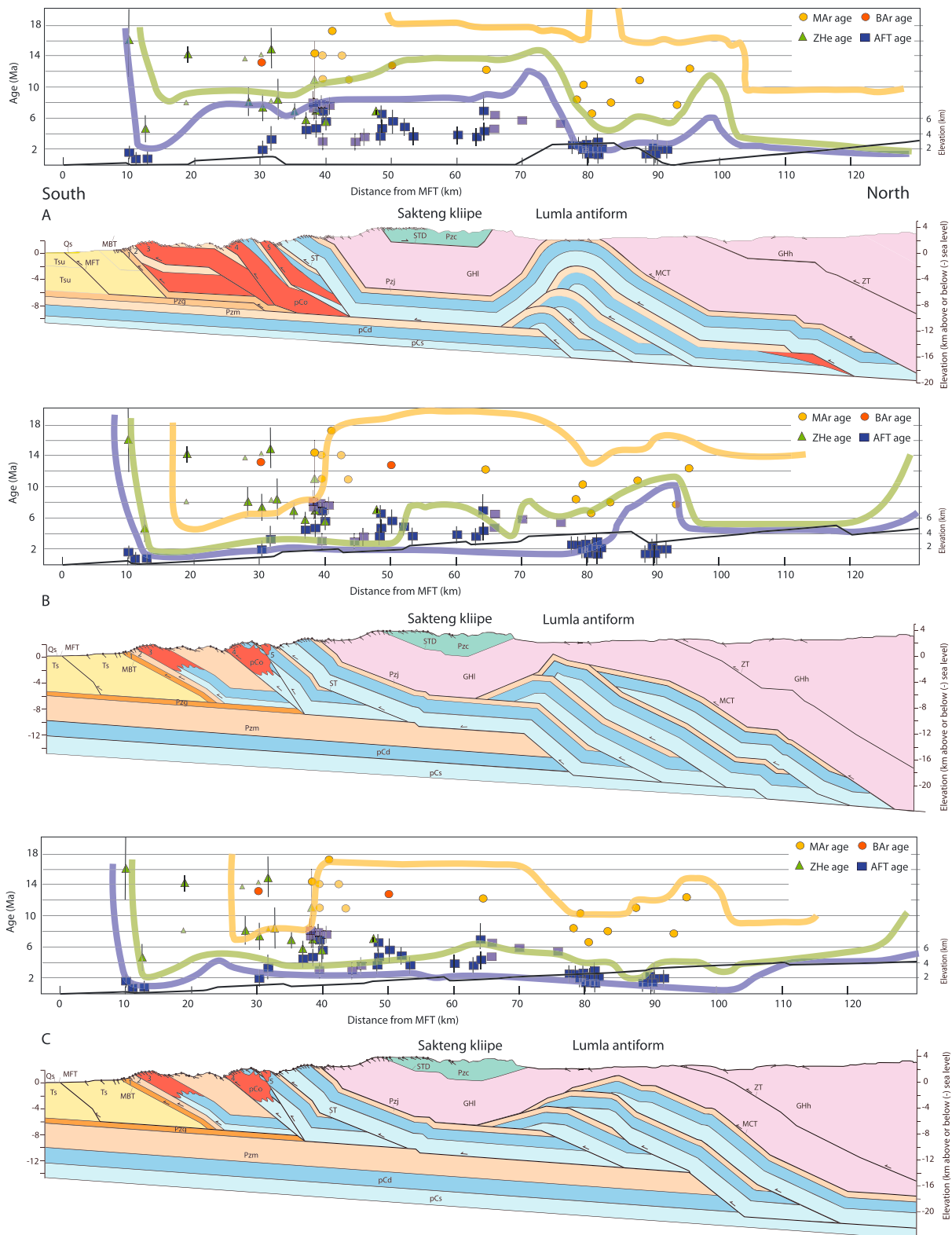


Figure 6. Predicted MAR (yellow), ZHe (green), and AFT (blue) cooling ages for cross sections A, B, and C using a constant velocity of 17.5 mm/year and an A_0 value of $3.0 \mu\text{W}/\text{m}^3$. The width of the lines representing the predicted cooling ages is 1 Myr. Predicted topography is indicated by black line. Transparent data symbols represent data that are greater than 20 km from the line of section, and small ZHe symbols represent single-grain ages not included in the mean age (see Table 1).

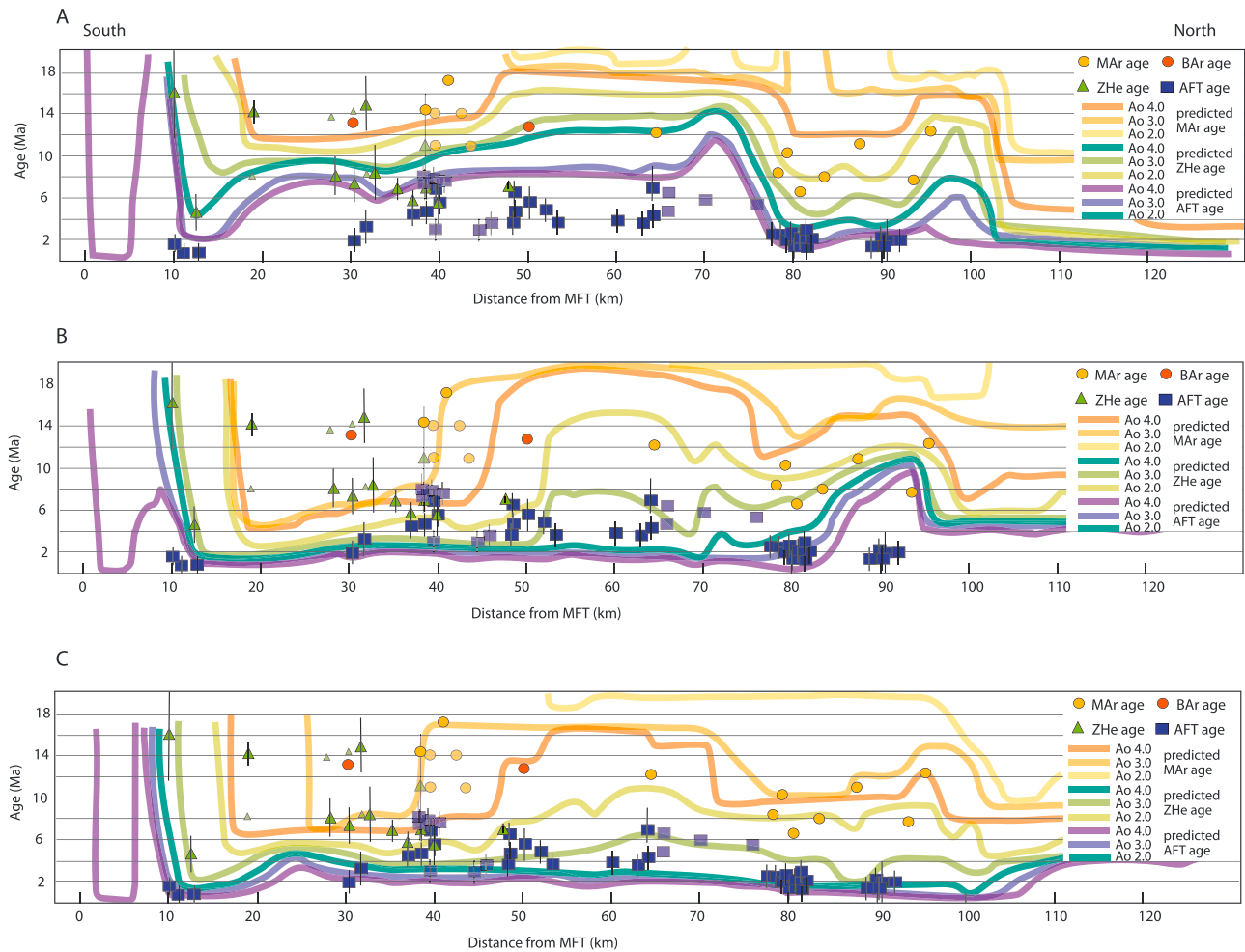


Figure 7. Predicted MAR (oranges), ZHe (greens), and AFT (blues) cooling ages compared to published data using variable surface heat production (A_0) values ($\mu\text{W}/\text{m}^3$) for cross sections A, B, and C (Figure 4) using a constant velocity of 17.5 mm/year.

Because of the more northerly position of the active ramp in cross section C, the young predicted AFT ages extend from 30 to 100 km north of the MFT, providing a match to the young measured ages in the region of the ZT. The notable change in the predicted ZHe signal in cross section B versus C between 50 and 90 km north of the MFT is also due to the northward extent of the ramp and the associated cooling. In cross section C, the ZHe ages no longer reflect the southward younging duplex, but rather the exhumation associated with the northward migrating ramp, superimposed on two previous pulses of exhumation—formation of the imbricate fan and formation of the duplex. This creates an exhumation low (and thus older predicted ages) in the Sakteng klippe. The oldest predicted ZHe age in the Sakteng klippe (6.4 Ma) is the age of initiation for the second LH thrust (Figure 6) and formation of the active ramp (Figures 5n–5p). Thus, the predicted ZHe ages get younger toward that active ramp. In this model the LH duplex formed between 13.5 and 10 Ma, assuming a constant shortening rate of 17.5 mm/year. The deformation and associated exhumation of the duplex is seen in the southward younging 13–10-Ma predicted MAR ages in the Lumla antiform 80–100 km north of the MFT. Similar to the predicted ages from cross section B, cross section C produced MAR ages that match measured ZHe ages between 25 and 35 km north of the MFT. Cross section C also produced the best match for the three young (1–2 Ma) AFT ages and the older ZHe ages ~10 km from the MFT.

6.3. Effect of Thermal Properties: Results

To evaluate the effect of changing thermal properties on the predicted ages generated from the three different cross-section geometries we show a suite of predicted ages that result from model runs using A_0 values of

2.0, 3.0, and 4.0 $\mu\text{W}/\text{m}^3$ (Figure 7). As expected, and as shown in previous studies (Gilmore et al., 2018; McQuarrie & Ehlers, 2015), using a higher heat production produces younger ages. Also significant is that the first-order shape of the across-strike predicted ages illustrated in Figure 6 does not change, and still reflects the geometry of the cross section and the different windows of time that structures are active. What does change with changing heat production is the chronometer that records the geometry and rate of deformation and the age of the predicted chronometer. For example, in all three cross sections, the lowest surface heat production value used for AFT ages ($A_0 = 2.0 \mu\text{W}/\text{m}^3$) records the exact same cooling pattern as the highest value used for ZHe ages ($A_0 = 4.0 \mu\text{W}/\text{m}^3$). In cross sections B and C the cooling pattern highlighted by the AFT ages ($A_0 = 3.0$ and $4.0 \mu\text{W}/\text{m}^3$) is markedly different than the cooling pattern highlighted by ZHe ages ($A_0 = 3.0$ and $4.0 \mu\text{W}/\text{m}^3$). The identical cooling pattern of AFT ages with $A_0 = 2.0$ and ZHe ages with $A_0 = 4.0 \mu\text{W}/\text{m}^3$ indicates that the rocks at the model surface in these two sections are at a critical thermal threshold where, when exhumed through a low thermal gradient, the rocks will preserve a different cooling age pattern than if that same exhumation occurred through a higher thermal gradient. Thus, if the across-strike pattern of predicted cooling ages for one chronometer is the same as the measured ages recorded by cooler (or warmer) one, it does not necessarily indicate a fundamental problem with the model. Rather, it indicates that the pattern of cooling imparted by the structures is viable and requires a change in heat production or the magnitude of exhumation for the correct chronometer to record that signal.

In all three cross-section models, changes in A_0 have the smallest effect on predicted AFT cooling ages for the range of A_0 values tested. In cross sections B and C the predicted AFT ages, regardless of heat production values, are controlled by the motion of rocks over the active ramps located ~ 70 – 80 km (section B) and 95 – 105 km (section C) north of the MFT (Figure 7). The chronometer that is most sensitive to change in heat production is ZHe. Smaller incremental changes of heat production ($0.2 \mu\text{W}/\text{m}^3$) showed the largest effect on the predicted ZHe ages with the predicted ages decreasing by 0.5 Ma with each 0.2 increase in A_0 .

6.4. Effect of Velocity: Results

Changing the model from a constant velocity of 17.5 mm/year to one in which velocity varies with time changes both the absolute age of a given thermochronometer, as well as the amplitude of curves or slope (age versus distance) of the across-strike pattern in predicted ages (Gilmore et al., 2018; McQuarrie & Ehlers, 2015). The slope of age versus distance for predicted AFT ages from cross section C is highlighted in Figure 6 as a very shallow slope from 3 Ma at 28 km north of the MFT to 0.5 Ma at 100 km north of the MFT. The measured ages also define a southward dipping slope in age/distance space; however, it is notably steeper with ages as old as 7.5 to 5 Ma located ~ 40 km north of the MFT. The difference between predicted and measured ages argues for a slower rate than 17.5 mm/year between 7 Ma and present as proposed in previous studies (Gilmore et al., 2018; Long et al., 2012; McQuarrie & Ehlers, 2015). We use cross section C to evaluate the sensitivity of AFT and ZHe ages to slower rates than 17.5 mm/year from ~ 8 Ma to present by comparing the predicted ages using rates of 17.5 , 10 , and 7.5 mm/year over the last 7 to 10 Myr (Figures 8a and 8b). As expected, the slower velocities increase the age and slope. The 7.5 -mm/year rate produced predicted AFT ages that matched the oldest measured ages between 40 and 90 km north of the MFT. This slow rate also predicted ZHe ages that are 2.5 to 4 Myr older than the measured ages between 25 and 40 km north of the MFT. The rate of 10 mm/year in the last 7.5 Myr produced predicted ages that match the median AFT ages (Figure 8a). In addition, the predicted ZHe ages match the measured ages (Figure 8b).

To have slow shortening rates in the last ~ 7.5 Myr without forcing the previous deformation ages to be 4 to 6 Myr older requires a period of time in which shortening was faster than 17.5 mm/year. For the models presented in Figure 8, we have increased shortening rates to 55 mm/year between 10 and 12 Ma before slowing to 7.5 mm/year and between 7.5 and 9.5 Ma before slowing to 10 mm/year. The period of fast shortening is during emplacement of the LH thrust sheets (Figures 5m and 5n), similar to that proposed in previous shortening rate models for Bhutan (Gilmore et al., 2018; Long et al., 2012; McQuarrie & Ehlers, 2015). Even with the 2 Myr of faster rates, slower rates in the last ~ 7.5 Myr also predict older MAr ages because the slower rates shift the absolute age of deformation older for all previous structures. The model that most closely predicts the measured MAr ages in the region of the Sakteng klippe and to the north (40 – 100 km north of the MFT) is the constant velocity model that has duplex formation from 12.5 to 10 Ma (Figure 8c). Even though the model with a recent (7.5 – 0 Ma) shortening rate of 10 mm/year also has duplex formation from 12.5 to 10 Ma, the predicted MAr cooling ages are 1 Myr

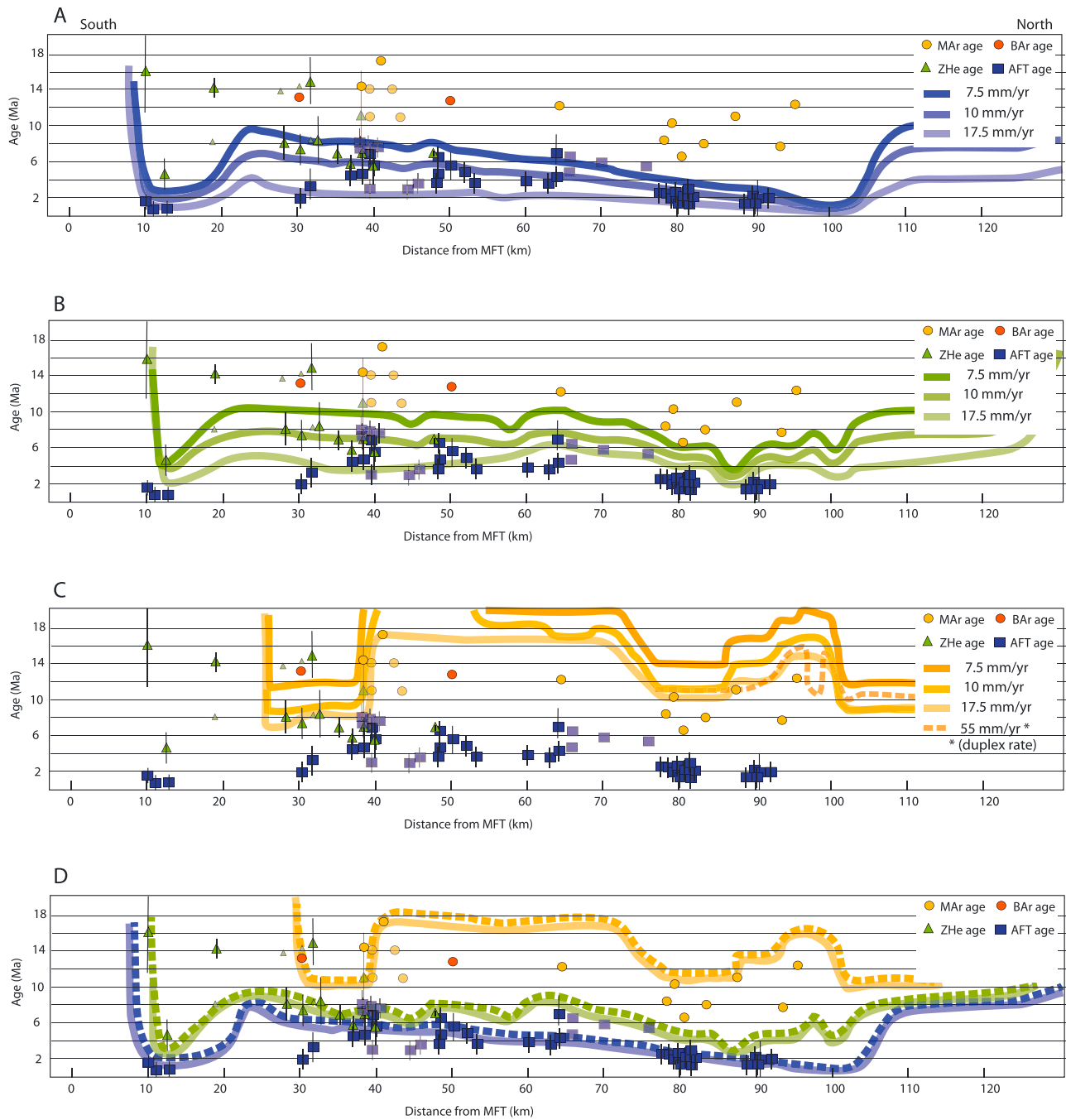


Figure 8. Predicted cooling ages using three different velocities from 7–10 Ma to present and an A_0 value of $3.0 \mu\text{W}/\text{m}^3$ for cross section C. (a) Predicted AFT ages, (b) predicted ZHe ages, and (c) predicted MAR ages. Dashed orange line shows change in age if LH duplex formation occurs at a rate of 55 mm/year. (d) Predicted MAR (yellow), ZHe (green), and AFT (blue) cooling ages assuming rates of 10 mm/year (0–9.5 Ma), 55 mm/year (11.3–9.5 Ma), and 20 mm/year (11.3–16 Ma) shown in the dashed lines and compared to the same rates, but with faster shortening (17 mm/year) between 0.8 Ma and the present shown with solid lines.

older. This age difference highlights that the final cooling age is more than just the age and rate of the structures that facilitate the initial deformation and exhumation. The subsequent faster rate of cooling as the duplex is uplifted over an active ramp at a rate of 17.5 mm/year produces younger MAR ages. This effect is highlighted in Figure 8d; in this scenario the age and rate of deformation is exactly the same except for the last 1 Myr. The older set of predicted ages is a function of shortening at 10 mm/year over 1 Myr. The younger set of ages results from a shortening rate of 17 mm/year over the last

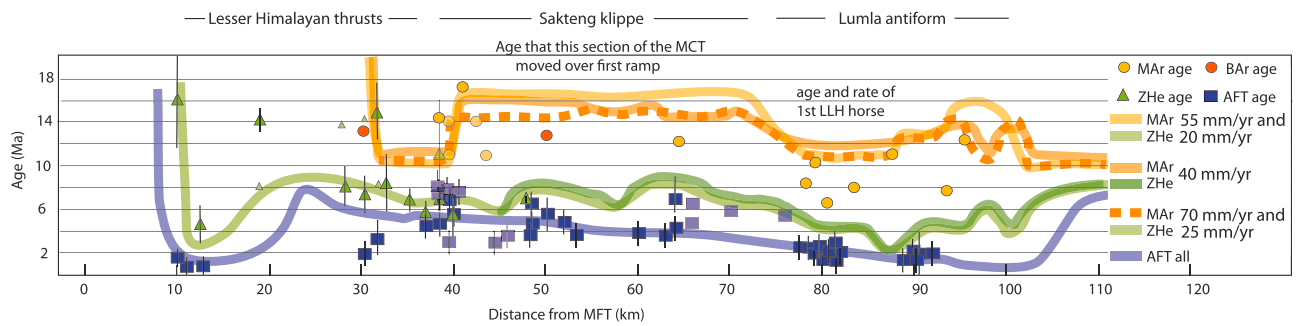


Figure 9. Plot of best fit velocities showing predicted MAR (oranges), ZHe (greens), and AFT (blue) ages compared to measured ages. All velocities have a rate of 17 mm/year for the last 0.8 Myr and 9.5–10 mm/year from 0.8 to 8 Ma. These rates control the shape of the blue AFT curve. The different shading for MAR and ZHe ages reflects different speeds for the LH thrusts that make up the first horse in the duplex (20–25 mm/year from 10.6 to 14 or 16 Ma) and the next five faults in kinematic order (e.g., Figures 5m and 5n) moving at a rate of 45–70 mm/year from 8 to 10.6 Ma. The orange and green lines corresponding to 40 mm/year represent a constant 40-mm/year rate from 8 to 16 Ma. LLH refers to lower Lesser Himalayan rocks in duplex.

0.8 Myr. The change in rate over this window of time makes all previous deformation ages younger by 0.5 Ma.

The rate of shortening and cooling during duplex formation changes the age and range of predicted MAR ages between 75 and 100 km north of the MFT. At slow rates, the predicted ages form a north sloping pattern of increasing ages that extend from the oldest ages (in the north) that are the same as those predicted for the Sakteng klippe (40–75 km from the MFT) to ~5 Ma younger in the region of the Lumla antiform (80–100 km from the MFT; Figure 8c). At faster rates that range in age narrows, and at the fastest rates (55 mm/year), the pattern loses the middle step in predicted ages that are a function of successive active ramps during duplex formation (Figure 8c).

Through combining the suite of observations of how velocity affects predicted ages, we propose a best fit velocity for the best fit geometry of cross section C. The best fit velocity retains the slower rate of 9.5–10 mm/year for the last 9 Myr, with a period of faster shortening (at modern GPS rate) from 0.8 Ma to present. To produce the best match to the younger MAR ages measured at the southern edge of the Sakteng klippe, as well as in the Lumla antiform, velocities from 9 to 9.5 Ma are 45 mm/year, and increase to 70 mm/year from 9.5 to 10.7 Ma. Slower velocities (25 mm/year) from 10.7 to 14 Ma allow for a northward slope of predicted ages as seen in the measured MAR ages. However, even with the fast shortening rates (45–70 mm/year), the predicted ages only match the oldest measured ages (Figure 9). A fast rate again (55 mm/year) from the time that the MCT carried the Sakteng klippe over its initial footwall ramp (15.5 to 14 Ma) controls the predicted ages in the klippe and the predicted ages at ~100 km north of the MFT. An earlier age for MCT initiation (20 Ma) is possible if the amount of displacement on the MCT was greater (allowing the Sakteng portion of the thrust sheet to be exhumed at ~15 Ma).

Slightly slower velocities (than 70 mm/year) during emplacement of the LH thrust sheets, 55 mm/year from 9 to 10.8 Ma, and 20 mm/year from 10.8 to 16 Ma still provide the same fit for the predicted MAR ages between 75 and 90 km north of the MFT, but the older age of MCT motion predicts 17-Ma ages across the Sakteng klippe. Both 70 and 55 mm/year are faster than plate tectonic rates (~40–45 mm/year) at this time (Copley et al., 2010). To evaluate the sensitivity of these rates we also modeled shortening rates of 40 mm/year from 9 to 16 Ma (Figure 9). Similar to the faster rates, the age for MCT motion (16 to 13 Ma) controlled the age in the Sakteng klippe, and the initial age of duplex formation (12.5–12 Ma) controlled the predicted ages (~12 Ma) between 75 and 95 km north of the MFT. The older predicted ages miss all of the measured ages in this region by 1–2 Myr (Figure 9).

7. Discussion

7.1. Matching Highly Variable Measured MAR and AFT Ages

MAR ages from GH rocks south of the Sakteng klippe and in the immediate MCT hanging wall range from 11.0 ± 0.4 to 17.05 ± 0.6 Ma. The along-strike (roughly east-west) map distance is 40 km between the farthest

samples (Figure 2); samples proximal to the section line range from 14.4 to 17.05 Ma, while the samples located the farthest to the west display an age range from 11.0 to 14.1 Ma, indicating potentially higher exhumation or more recent exhumation there. The across-strike distance when projected onto the line of section is ~5 km. Although the elevation difference between the samples ranges from 1,060 to 2,540 m, there is no correlation between sample age and elevation (for example, two samples that yield 14.1- and 11.1-Ma ages are less than 0.5 km apart in the immediate hanging wall of the MCT; Figure 2). The 3-Myr range in ages (for each set of samples) is significantly larger than the uncertainties on individual measurements. A similar spread in ages (3–4 Myr) is seen in the measured MAr ages in the Lumla antiform (6.5 to 10.3 ± 0.2 Ma; Figures 2 and 4). There is no reason that these samples should have experienced different peak temperatures or time at peak temperature. Looking at similar rocks in Sikkim India, directly west of Bhutan, Mottram et al. (2015) showed that muscovite single-grain ages had a significantly larger age spread (2–5 Ma) that was not seen in MAr plateau ages; thus, the range in measured ages represents a geological uncertainty that is not as yet understood. The dispersed age range in our MAr data prevents us from matching our predicted ages to all of the measured ages. Therefore, to be conservative in geometry and rate, we consider matching the older ages (~14 Ma south of the Sakteng klippe and 10–11 Ma in the Lumla antiform) a good fit. As mentioned in section 6.3, younger predicted MAr ages are only possible with faster rates from ~9 Ma to present (which predicts AFT and ZHe ages that are 2–4 Myr younger than measured ages), or rates faster than 55–70 mm/year from ~12 to 9 Ma.

The wealth of AFT ages through this region shows both a clear trend in the cooling signal as well as scatter that spans 3–4 Myr. Although part of that scatter may be location-dependent (the measured ages span an across-strike distance of 70 km), plotting age variations from a narrowed geographical area (~10-km diameter), the age variation of ~3–4 Ma persists and shows no correlation to changes in elevation or distance from structures. Thus, for our fits to the AFT ages, our best fit match between predicted and measured ages passes through the center of the range of measured ages (Figure 9).

7.2. Control of Geometry on Cooling Ages

Although the young active duplex geometry (75–95 km north of the MFT) of cross section A provides a mechanism to produce the 1–2-Ma AFT ages measured here, the last structure to facilitate uplift and exhumation for the LH thrusts (20–40 km N of the MFT) and the Sakteng klippe (40–70 km north of the MFT) was motion over a LH ramp currently located 115–120 km north of the MFT (Figure 6). Assuming a constant shortening rate of 17.5 mm/year, this exhumation occurred from 10 to 8.5 Ma for the LH thrust sheets (Figure 5c) and from 8.5 to 8 Ma for the Sakteng klippe. These periods of cooling are seen in the predicted ZHe ages for thrusts, and the AFT ages predicted for the Sakteng klippe. Thus, the only way to make these predicted ages as young as the measured ages is to have rapid shortening from 2 to 5 Ma (~60 mm/year) so that the motion of the thrust sheets over the ramp occurred at 5 Ma and with exhumation of the Sakteng klippe following at 4 Ma. These rapid rates have the benefit of also predicting younger MAr ages (similar to the 14–12-Ma ages measured in the region). However, the predicted ZHe ages become distinctly younger (4–5 Ma) than the 6–8-Ma measured ages 25–40 km north of the MFT. The mismatch of the measured to predicted ZHe ages and the viability of having rapid shortening rates from 2 to 5 Ma both argue that the geometry for cross section A is incorrect.

The active ramps in cross sections B and C both provide a mechanism for producing the young measured AFT ages sampled across GH rocks and the associated Sakteng klippe. These ages that broadly get younger moving from 35 and 95 km north of the MFT are consistent with continued displacement of rocks toward the south over an active décollement ramp from 8 Ma to present. The northward location of the youngest AFT ages provides a strong constraint on the location of this ramp. By comparing the predicted AFT ages between cross sections B and C (Figure 6), the top of the active décollement ramp must be at least as far north as 85 km from the MFT to produce the young AFT age measured at 90 km and indicates that the geometry shown in cross section C is more correct. The exact position of the ramp could be constrained by AFT and ZHe ages collected between 95 and 115 km north of the MFT. These potential ages would be predicted to record the progressive increase in ages where rocks have not been transported over the ramp.

The amount of exhumation in the Lumla window, as indicated by the 6.5–12-Ma MAr ages, emphasizes the need for multiple pulses of exhumation in this region. Comparing the predicted MAr ages from cross sections A, B, and C highlights controls on the cooling ages in each section. Even with an active duplex in

cross section A, the age and magnitude of exhumation is insufficient to yield reset MAR ages. The predicted MAR signal is a function of cooling associated with motion on the MCT from 18 to 16 Ma (Figure 6). With high heat production, additional exhumation of the duplex produces younger ages, but only by 4 Myr (Figure 7). For cross section B, the MAR predicted ages between 75 and 90 km north of the MFT show the southward younging signal expected from a hinterland dipping duplex. The 13–17-Ma predicted ages are slightly older than the age of duplex formation (11–15 Ma). A higher heat production value makes these predicted ages directly reflect the ages of duplex formation (11–15 Ma), but they still fall short of being as young as the measured ages in this region (Figure 6). The geometry of cross section C, with exhumation over an active ramp superimposed on the initial exhumation associated with duplex formation, does produce predicted ages as young as measured ages in the region (Figures 6 and 9).

Accounting for the range in published ages, and partial resetting of ZHe ages between 15 and 35 km north of the MFT (section 3.2), our best fit geometry and velocity model is able to match 50% of the measured MAR ages, 80–100% of the ZHe ages, and 73% of the AFT cooling ages. The samples that are notably not reproduced by our preferred geometry and velocity models are the youngest MAR ages, particularly in the region of the Lumla window and the two young AFT ages ($1.7 + 1.3/ - 0.7$ and $3.2 + 1.8/ - 1.2$ Ma) between 30 and 33 km north of the MFT. These young ages fall off the age-distance trend of the other AFT samples. The predicted AFT cooling ages just intersect the upper end of the error bar for the oldest (3.2 Ma) age. The associated ZHe ages cluster at ~8 Ma, which is consistent with the other ZHe ages from the region. Therefore, any additional exhumation that has yielded the younger, 2–3-Ma AFT ages was not sufficient to affect the related ZHe ages. The best fit model also misses the four Grujic et al.'s (2006) AFT ages collected along the river between Trashi Yangtse and Trashigang between 65 and 75 km from the MFT (Figure 2). These ages (while also decreasing to the north) are 2–3 Myr older than the AFT ages along the line of section. The model fits 100% of the ZHe data if the young age component of samples BU12-81B, 98B, 76B, and 74B are taken into account. If only the weighted mean of the two similar ages is considered, there is an 83% match.

7.3. Relation Between Geometry and Final Predicted Topography

The predicted topography from the different cross-section geometries, compared to the actual topography of the cross section (Figure 6), also provides insight into the geometric viability of the sections. Our method for estimating the topography through time connects the increase of topographic elevation with structures that generate uplift. A significant mismatch between the measured topographic profile and the reconstructed topographic profile can invalidate cross-section geometry and kinematics.

As illustrated in Figure 5 and discussed previously, the kinematics of cross section A has the LH thrust sheets deform early before translation over the active ramp through LH rocks. This uplift was the last period of active uplift for the Sakteng klippe, after which it was passively translated along a flat. The topography generated during this period of deformation (Figure 5c) gradually subsided during translation (Figures 5d and 5e). Active duplex formation north of the Sakteng klippe and motion along the MBT and MFT both created topography to the north and south of the Sakteng klippe but the predicted topography in the region of Sakteng is at sea level (Figure 6a). The predicted topography is almost a direct inverse of the actual topography between 35 and 100 km north of the MFT. The predicted topography from cross section B is a better match to the topographic profile; however, there are still some notable differences. The most significant difference, similar to cross section A, is that the active uplift under the Lumla antiform produces the highest predicted topography along the profile. This contrasts with the higher actual elevations in the Sakteng klippe as well as the higher elevations to the north of the Lumla antiform. This mismatch of topography, combined with the inability of the cross section to match the young AFT ages 90 km north of the MFT, indicates that the active ramp must be farther to the north. A significant difference between the predicted and actual topography shared by all three cross sections is the dramatic topographic rise immediately north of the MBT. Here elevations go from 200 m to 2 km over a distance of ~5 km. All of our predicted topographies show this region as 0 km in elevation (cross section A) or at the most a few hundred meters (cross sections B and C). Twenty kilometers north of the rapid elevation gain at the MBT are the young AFT ages that are also poorly matched by the cross-section geometries. We hypothesize that out-of-sequence motion on the MBT can reproduce the topography as well as provide a match to the young AFT ages. Modeling out-of-sequence motion on the MBT that moves 6 km at a rate of 17 mm/year following

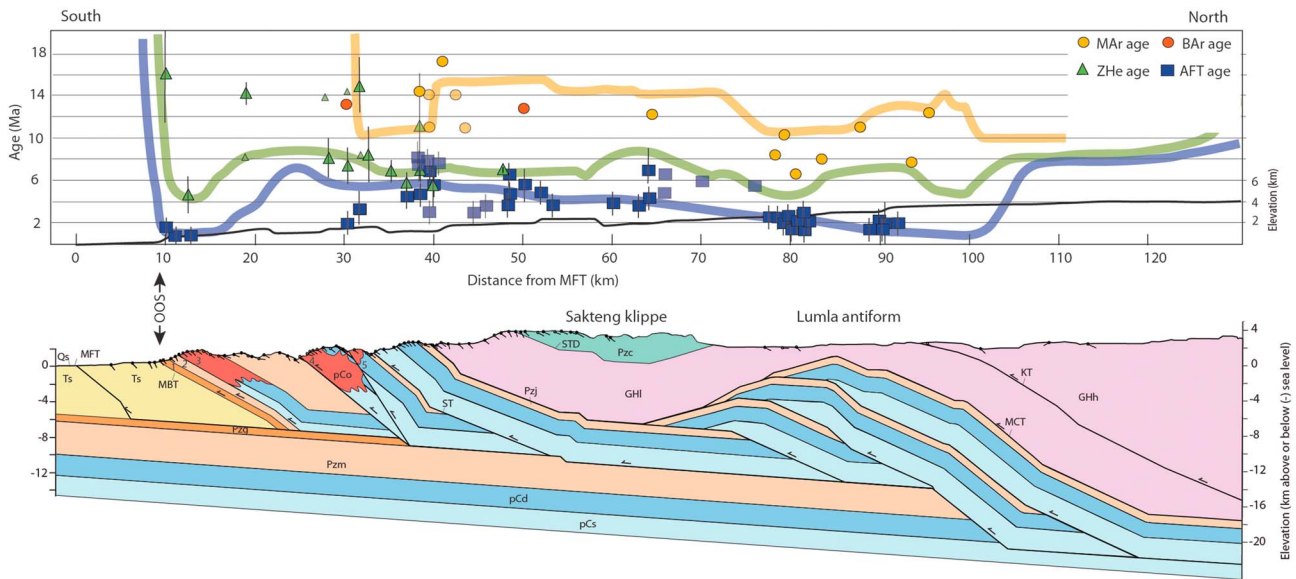


Figure 10. Plot of predicted MAr (yellow), ZHe (green), and AFT (blue) ages compared to measured ages for out-of-sequence (OOS) fault model (cross section C) with OOS fault located at the MBT. Thin black line is the predicted elevation assuming a 4° slope from the MFT to 20 km to the north during OOS motion and a 2° slope from 20 to 140 km north of the MFT.

motion on the MFT does provide a better match to topography, but only slightly alters the predicted AFT ages, making the fit to the measured 3.2 Ma age stronger, but still completely missing the 1.7-Ma age (Figure 10). Due to a décollement depth of 6–7 km in this location, it is unlikely that a higher fault displacement amount will produce younger AFT ages.

7.4. Variability in Rates

The variability in rates proposed in our best fit velocity model shares common features with proposed estimates for the age and rate of deformation for this region. In particular is the marked slowdown in shortening rates (Gilmore et al., 2018; Long et al., 2012; McQuarrie & Ehlers, 2015) and exhumation rates (Coutand et al., 2014) from ~6–8 Ma to the present (Figure 11). The transect evaluated here is the third cross section

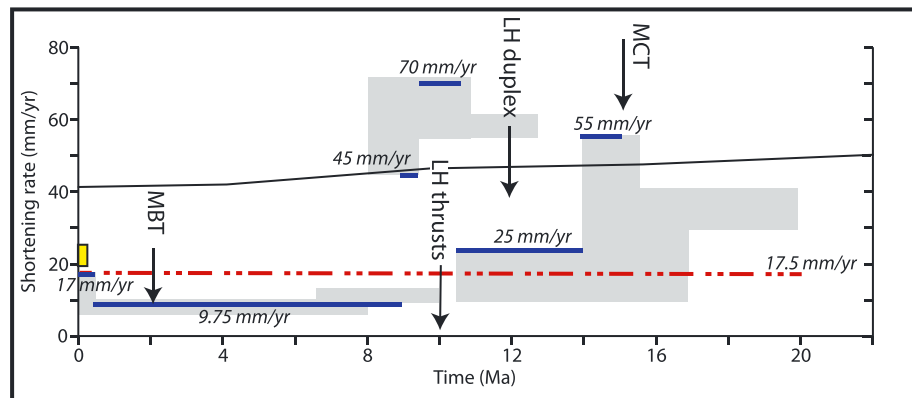


Figure 11. Graph of horizontal shortening rate versus time, showing changes in shortening rates accommodated by the Bhutan fold-thrust belt for this study (thick blue lines) and permissible velocities for cross sections modeled to the west (Gilmore et al., 2018; McQuarrie & Ehlers, 2015) in gray boxes. The thin black line shows overall India-Asia convergence rate (from Copley et al., 2010), and the red dash-dotted line is the constant shortening rate from 20 Ma to present. The yellow box shows range of global positioning system (GPS) convergence rates for the eastern Himalayan thrust belt (~20–25 mm/year; Banerjee et al., 2008). Vertical arrows indicate initial motion on major structures in our best fitting model. MBT is the Main Boundary thrust, MCT is the Main Himalayan thrust, and LH is the Lesser Himalayan.

from eastern Bhutan where kinematics from a balanced cross section have been integrated with advection-diffusion thermokinematic models to constrain geometry, kinematics, and rates of thrusting (Gilmore et al., 2018; McQuarrie & Ehlers, 2015). The associated cross sections span an across-strike distance of 70 km, over which there are pronounced changes in the outcrop expression of mapped geology (Long, McQuarrie, Tobgay, Grujic, & Hollister, 2011; Figure 2). Yet even with notable changes in mapped geology, cross-section geometry, and cooling ages (Long, McQuarrie, Tobgay, & Grujic, 2011, 2012; this study), the proposed variations in velocity to best fit measured cooling ages remain remarkably consistent. Within the range of acceptable velocities, all three cross sections require slow rates (7–10 mm/year) over the last 6–9 Myr, with permissible faster rates (14 mm/year) from 6 to 10 Ma (Gilmore et al., 2018) or 17 mm/year from 0.8 Ma to the present (this study). All three cross sections require faster than plate convergence rates from ~8 to 12 Ma, with preferred rates as high as 55–75 mm/year (McQuarrie & Ehlers, 2015; Gilmore et al., 2018; this study). Rates faster than plate tectonic rates are only permissible with coeval extension on the STD (Gilmore et al., 2018; McQuarrie & Ehlers, 2015). A 12.5-Ma Th–Pb monazite age from Kula Kangri (at the border of Bhutan and Tibet) and 7-Ma ZHe ages (Coutand et al., 2014; Edwards et al., 1996; Edwards & Harrison, 1997) indicate STD displacement from 7 to 12 Ma, the same time window of rapid shortening proposed for eastern Bhutan.

7.5. Control of Duplex Formation on Uplift and Exhumation

Rapid (2–4 mm/year) and young (<10 Ma) exhumation is identified in multiple locations along the Himalayan orogen, and is shown to vary in both time and space (e.g., Thiede & Ehlers, 2013). These temporal and spatial variations highlight the importance of identifying the drivers of uplift, which by inference also must be changing in time and space. Fold-thrust belt kinematics, in particular how ramps are created and systematically move toward the hinterland (with respect to the frontal structures) as overlying rocks are displaced toward the foreland, provide a template for spatially and temporally evolving uplift. The location and magnitude of footwall ramps (i.e., the footwall cutoff of a thrust fault) that migrate toward the hinterland all have corresponding foreland thrust faults (i.e., the resultant hanging wall cutoff) that are preserved in the front of the system. This link between foreland structures and hinterland ramps can be exploited to create a series of testable cross-section geometries (Figure 6) that all match the geology at the surface but provide different subsurface geometries and thus different uplift histories. In particular, active uplift in the hinterland of the Himalayan fold-thrust belt has been proposed to be a function of an active duplex (Adams et al., 2013, 2016; Landry et al., 2016; Webb et al., 2011, 2013), out-of-sequence thrusting (Adlakha et al., 2013; Wobus et al., 2003, 2006), and an active ramp in the décollement (Bollinger et al., 2006; Gilmore et al., 2018; Herman et al., 2010; Long et al., 2012; Robert et al., 2011). These different driving mechanisms predict different uplift, exhumation, and topographic evolutions, which can be directly compared to measured thermochronometers and modern topography. We evaluated an active duplex as a driver for uplift on the Sakteng–Daifam transect using cross section A. Although active duplex formation definitely produces uplift and exhumation in the region of duplex formation, it also strongly limits any recent exhumation and the generation of structural elevation of the region directly to the south (Sakteng klippe) due to the kinematics of duplex formation. The requirement of emplacing a roof thrust over a duplex (Figures 5d and 5e) makes the topographic uplift and exhumation of the rocks immediately south of the duplex notably older (Figure 6). In addition, isostatic loading from duplex growth also inhibits growth of topography to the north and south. While out-of-sequence faulting also can produce young ages, the thermochronologic and topographic response of out-of-sequence faulting is notably younger ages and a marked increase in topography in the hanging wall (Wobus et al., 2003) and more subdued topography in the immediate footwall (Gilmore et al., 2018; Figure 10). These observations do not hold true either at the trace of the MCT or on the southern limb of the Lumla antiform (Figure 6), indicating that an out-of-sequence fault is not a valid uplift and associated exhumation driver for this location. An active ramp produces the pattern of increasingly younger AFT ages from the trace of the MCT to north of the Lumla antiform, but only if it is in the correct location (Figures 6b and 6c). In addition, uplift driven by an active décollement ramp is the geometry that most accurately reproduces the topography of the region (Figure 10). The approach that we outline here has the potential to dramatically increase our understanding of the relationships between deformation geometry and rates and the resulting exhumation and evolution of topography, thus providing tools to more quantitatively evaluate the competing controls that climate-driven erosion and uplift-driven exhumation exert on the topographic evolution of orogenic belts.

8. Conclusions

New and published MAR, ZHe, and AFT ages combined with mapping and viable cross-section geometries facilitate testing the geometry, kinematics, and rate of deformation in eastern Bhutan. The mismatch of predicted to measured cooling ages allows us to invalidate the geometries shown in cross sections A and B (Figure 4). Changing the rate and order in which faults move in cross section C results in a strong match between predicted and measured ages. MAR ages that range from 17 to 11 Ma require that the MCT was deforming at rates of 40–55 mm/year from at least 16 to 14 Ma. Displacement on the frontal parts of the MCT continued as the LH duplex grew from ~12 to 10.5 Ma. Emplacement of frontal LH thrust sheets occurred rapidly (55–70 mm/year) between ~11 and 9 Ma. The out-of-sequence ZT is proposed to have two periods of displacement before and after motion on the frontal LH thrust sheets at ~10 and 8 Ma. Motion on the MBT was significantly slower than previous velocities, at ~10 mm/year from 7 to 0.5 Ma with modern rates of motion (17 mm/year) in the last 0.5 Myr. High topography and young AFT ages near the MBT indicate out-of-sequence motion on this structure. The models presented in this study support previous work that argued for a pronounced decrease in shortening rates (7–10 mm/year) and associated exhumation at ~8 Ma, following a period of much faster shortening from ~8 to 12 Ma. The data that require these variable rates are AFT ages as old as 5–7 Ma near the trace of the MCT, older ZHe ages (~7–8 Ma), and relatively young (14–8 Ma) MAR ages.

We emphasize that understanding the progression and geometry of foreland deformation in a thrust belt is critical for understanding how to interpret cooling ages, both for foreland structures and the resulting location and magnitude of hinterland ramps. Although we have used the Himalayan fold thrust belt to develop and test this approach, its applicability is relevant to any active orogen and has the potential to assess climatic versus tectonic rejuvenation in recent orogens. In particular, the geometry and resulting kinematics of deformation produces a pattern of topographic uplift, exhumation, and predicted cooling ages that can be directly compared to measured ages and modern topography. Although the geometry sets the first-order pattern of exhumation, the magnitude of exhumation, and thus which chronometer records a particular cooling event, is a function of the amount of erosion that occurs. The location and magnitude of modern and past ramps, combined with the topographic evolution of the thrust belt, exert the strongest controls on the across-strike pattern of cooling ages.

Acknowledgments

We would like to thank the government of Bhutan for their assistance and support for field access and data collection, Peter Reiners and the University of Arizona Radiogenic Helium Dating Laboratory for the assistance and discussion regarding the zircon (U-Th)/He ages, and Willi Kappler for the assistance in the simulations presented in this manuscript. We acknowledge financial support from the European Research Council (ERC) Consolidator Grant (615703) to T.A. Ehlers and NSF EAR 0738522 to N. McQuarrie and the Alexander von Humboldt Foundation to P.R. Eizenhöfer and N. McQuarrie. We acknowledge Midland Valley (now Petex) for the use of the program *Move*. Devon Orme, Willy Guenther and an anonymous reviewer are thanked for their constructive comments that helped improve the manuscript. Any use of trade, firm, or product names is for descriptive purposes only and does not imply endorsement by the U.S. Government. The complete data sets used in this paper are available in the supporting files associated with this manuscript. The modified version of *Pecube-D* that can be coupled to 2-D *Move* restoration files is available through T.A. Ehlers.

References

- Adams, B. A., Hodges, K. V., van Soest, M. C., & Whipple, K. X. (2013). Evidence for Pliocene-Quaternary normal faulting in the hinterland of the Bhutan Himalaya. *Lithosphere*, 5(4), 438–449. <https://doi.org/10.1130/L277.1>
- Adams, B. A., Hodges, K. V., Whipple, K. X., Ehlers, T. A., van Soest, M. C., & Wartho, J. (2015). Constraints on the tectonic and landscape evolution of the Bhutan Himalaya from thermochronometry. *Tectonics*, 34, 1329–1347. <https://doi.org/10.1002/2015TC003853>
- Adams, B. A., Whipple, K. X., Hodges, K. V., & Heimsath, A. M. (2016). In situ development of high-elevation, low-relief landscapes via duplex deformation in the Eastern Himalayan hinterland, Bhutan. *Journal of Geophysical Research: Earth Surface*, 121, 294–319. <https://doi.org/10.1002/2015JF003508>
- Adlakha, V., Lang, K. A., Patel, R. C., Lal, N., & Huntington, K. W. (2013). Rapid long-term erosion in the rain shadow of the Shillong Plateau Eastern Himalaya. *Tectonophysics*, 582, 76–83. <https://doi.org/10.1016/j.tecto.2012.09.022>
- Banerjee, P., Bürgmann, R., Nagarajan, B., & Apel, E. (2008). Intraplate deformation of the Indian subcontinent. *Geophysical Research Letters*, 35, L18301. <https://doi.org/10.1029/2008GL035468>
- Barnes, J. B., Ehlers, T. A., Insel, N., McQuarrie, N., & Poulsen, C. J. (2012). Linking orography, climate, and exhumation across the central Andes. *Geology*, 40(12), 1135–1138. <https://doi.org/10.1130/G33229.1>
- Bhargava, O. N. (1995). *The Bhutan Himalaya: A geological account*. *Spec. Publ. Ser. Geol. Surv. India*, (Vol. 39, p. 245).
- Bhattacharyya, K., & Mitra, G. (2009). A new kinematic evolutionary model for the growth of a duplex—An example from the Rangit duplex, Sikkim Himalaya, India. *Gondwana Research*, 16(3-4), 697–715. <https://doi.org/10.1016/j.gr.2009.07.006>
- Bollinger, L., Henry, P., & Avouac, J. P. (2006). Mountain building in the Nepal Himalaya: Thermal and kinematic model. *Earth and Planetary Science Letters*, 244(1-2), 58–71. <https://doi.org/10.1016/j.epsl.2006.01.045>
- Braun, J. (2003). Pecube: A new finite-element code to solve the 3D heat transport equation including the effects of a time-varying, finite amplitude surface topography. *Computational Geosciences*, 29(6), 787–794. [https://doi.org/10.1016/S0098-3004\(03\)00052-9](https://doi.org/10.1016/S0098-3004(03)00052-9)
- Braun, J., van der Beek, P., & Batt, G. E. (2006). *Quantitative thermochronology*, (1st ed., p. 270). New York: Cambridge Univ. Press.
- Burchfiel, B. C., Zhiliang, C., Hodges, K. V., Yuping, L., Royden, L. H., Changrong, D., & Jiene, X. (1992). The south Tibetan detachment system, Himalayan orogen: Extension contemporaneous with and parallel to shortening in a collisional mountain belt. *Special Papers - Geological Society of America*, 269, 41.
- Chambers, J., Parrish, R., Argles, T., Harris, N., & Horstwood, M. (2011). A short-duration pulse of ductile normal shear on the outer South Tibetan detachment in Bhutan: Alternating channel flow and critical taper mechanics of the eastern Himalaya. *Tectonics*, 30, TC2005. <https://doi.org/10.1029/2010TC002784>
- Copley, A., Avouac, J.-P., & Royer, J.-Y. (2010). India-Asia collision and the Cenozoic slowdown of the Indian plate: Implications for the forces driving plate motions. *Journal of Geophysical Research*, 115, B03410. <https://doi.org/10.1029/2009JB006634>

- Corrie, S. L., Kohn, M. J., McQuarrie, N., & Long, S. P. (2012). Flattening the Bhutan Himalaya. *Earth and Planetary Science Letters*, 349–350, 67–74. <https://doi.org/10.1016/j.epsl.2012.07.001>
- Cottle, J. M., Waters, D. J., Riley, D., Beyssac, O., & Jessup, M. J. (2011). Metamorphic history of the south Tibetan detachment system, Mt. Everest region, revealed by RSCM thermometry and phase equilibria modeling. *Journal of Metamorphic Geology*, 29(5), 561–582. <https://doi.org/10.1111/j.1525-1314.2011.00930.x>
- Coutand, I., Barrier, L., Govin, G., Grujic, D., Hoorn, C., Dupont-Nivet, G., & Najman, Y. (2016). Late Miocene-Pleistocene evolution of India-Eurasia convergence partitioning between the Bhutan Himalaya and the Shillong Plateau: New evidences from foreland basin deposits along the Dungsam Chu section, eastern Bhutan. *Tectonics*, 35, 2963–2994. <https://doi.org/10.1002/2016TC004258>
- Coutand, I., Whipp, D. M. Jr., Grujic, D., Bernet, M., Fellin, M. G., Bookhagen, B., et al. (2014). Geometry and kinematics of the Main Himalayan Thrust and Neogene crustal exhumation in the Bhutanese Himalaya derived from inversion of multithermochronologic data. *Journal of Geophysical Research: Solid Earth*, 119, 1446–1481. <https://doi.org/10.1002/2013JB010891>
- Crowley, K. D., Cameron, M., & Schaefer, R. L. (1991). Experimental studies of annealing of etched fission tracks in fluorapatite. *Geochimica et Cosmochimica Acta*, 55(5), 1449–1465. [https://doi.org/10.1016/0016-7037\(91\)90320-5](https://doi.org/10.1016/0016-7037(91)90320-5)
- Dahlen, F. A. (1990). Critical taper models of fold-and-thrust belts and accretionary wedges. *Annual Review of Earth and Planetary Sciences*, 18(1), 55–99. <https://doi.org/10.1146/annurev.ea.18.050190.000415>
- Dahlstrom, C. D. A. (1969). Balanced cross sections. *Canadian Journal of Earth Sciences*, 6(4), 743–757. <https://doi.org/10.1139/e69-069>
- Daniel, C. G., Hollister, L. S., Parrish, R. R., & Grujic, D. (2003). Exhumation of the Main Central Thrust from lower crustal depths, eastern Bhutan Himalaya. *Journal of Metamorphic Geology*, 21(4), 317–334. <https://doi.org/10.1046/j.1525-1314.2003.00445.x>
- DeCelles, P. G., Carrapa, B., Gehrels, G. E., Chakraborty, T., & Ghosh, P. (2016). Along-strike continuity of structure, stratigraphy, and kinematic history in the Himalayan thrust belt: The view from Northeastern India. *Tectonics*, 35, 2995–3027. <https://doi.org/10.1002/2016TC004298>
- DeCelles, P. G., Kapp, P., Gehrels, G. E., & Ding, L. (2014). Paleocene-Eocene foreland basin evolution in the Himalaya of southern Tibet and Nepal: Implications for the age of initial India-Asia collision. *Tectonics*, 33, 824–849. <https://doi.org/10.1002/2014TC003522>
- DeCelles, P. G., Robinson, D. M., Quade, J., Ojha, T. P., Garzzone, C. N., Copeland, P., & Upreti, B. N. (2001). Stratigraphy, structure, and tectonic evolution of the Himalayan fold-thrust belt in western Nepal. *Tectonics*, 20(4), 487–509. <https://doi.org/10.1029/2000TC001226>
- DeCelles, P. G., Robinson, D. M., & Zandt, G. (2002). Implications of shortening in the Himalayan fold-thrust belt for uplift of the Tibetan Plateau. *Tectonics*, 21(6), 1062. <https://doi.org/10.1029/2001TC001322>
- Dodson, M. H. (1973). Closure temperature in cooling geochronological and petrological systems. *Contributions to Mineralogy and Petrology*, 40(3), 259–274. <https://doi.org/10.1007/BF00373790>
- Duncan, C., Masket, J., & Fielding, E. (2003). How steep are the Himalaya? Characteristics and implications of along-strike topographic variations. *Geology*, 31(1), 75–78. [https://doi.org/10.1130/0091-7613\(2003\)031<0075:HSATHC>2.0.CO;2](https://doi.org/10.1130/0091-7613(2003)031<0075:HSATHC>2.0.CO;2)
- Edwards, M. A., & Harrison, T. M. (1997). When did the roof collapse? Late Miocene north-south extension in the high Himalaya revealed by Th-Pb monazite dating of the Khula Kangri granite. *Geology*, 25(6), 543–546. [https://doi.org/10.1130/0091-7613\(1997\)025<0543:WDTRCL>2.3.CO;2](https://doi.org/10.1130/0091-7613(1997)025<0543:WDTRCL>2.3.CO;2)
- Edwards, M. A., Kidd, W. S. F., Jixiang, L., Yue, Y., & Clark, M. (1996). Multi-stage development of the southern Tibetan detachment system near Khula Kangri; New data from Gonto La. *Tectonophysics*, 260(1-3), 1–19. [https://doi.org/10.1016/0040-1951\(96\)00073-X](https://doi.org/10.1016/0040-1951(96)00073-X)
- Ehlers, T. A., Chaudhri, T., Kumar, S., Fuller, C. W., Willett, S. D., Ketcham, R. A., et al. (2005). Computational tools for low-temperature thermochronometer interpretation. *Reviews in Mineralogy and Geochemistry*, 58(1), 589–622. <https://doi.org/10.2138/rmg.2005.58.22>
- Ehlers, T. A., & Farley, K. A. (2003). Apatite (U-Th)/He thermochronometry: Methods and applications to problems in tectonic and surface processes. *Earth and Planetary Science Letters*, 206(1-2), 1–14. [https://doi.org/10.1016/S0012-821X\(02\)01069-5](https://doi.org/10.1016/S0012-821X(02)01069-5)
- Gansser, A. (1964). *Geology of the Himalayas*, (p. 289). New York: Wiley-Interscience.
- Gansser, A. (1983). *Geology of the Bhutan Himalaya*, (p. 181). Basel: Birkhäuser.
- Gavillot, Y., Meigs, A. J., Sousa, F. J., Stockli, D., Yule, D., & Malik, M. (2018). Late Cenozoic foreland-to-hinterland low-temperature exhumation history of the Kashmir Himalaya. *Tectonics*, 37, 3041–3068. <https://doi.org/10.1029/2017TC004668>
- Gilmore, M. E., McQuarrie, N., Eizenhöfer, P. R., & Ehlers, T. A. (2018). Testing the effects of topography, geometry and kinematics on modeled thermochronometer cooling ages in the eastern Bhutan Himalaya. *Solid Earth*, 9(1), 1–24. <https://doi.org/10.5194/se-9-1-2018>
- Gokul, A.R. (1983). Geological and mineral map of Bhutan. Hyderabad, India, Geological Survey of India Map Printing Division, scale 1:500,000, 1 sheet.
- Grujic, D., Coutand, I., Bookhagen, B., Bonnet, S., Blythe, A., & Duncan, C. (2006). Climatic forcing of erosion, landscape, and tectonics in the Bhutan Himalayas. *Geology*, 34(10), 801–804. <https://doi.org/10.1130/G22648.1>
- Grujic, D., Hollister, L. S., & Parrish, R. R. (2002). Himalayan metamorphic sequence as an orogenic channel: Insight from Bhutan. *Earth and Planetary Science Letters*, 198(1-2), 177–191. [https://doi.org/10.1016/S0012-821X\(02\)00482-X](https://doi.org/10.1016/S0012-821X(02)00482-X)
- Guenther, W. R., Reiners, P. W., Ketcham, R. A., Nasdala, L., & Giester, G. (2013). Helium diffusion in natural zircon: Radiation damage, anisotropy, and the interpretation of zircon (U-Th)/He thermochronology. *American Journal of Science*, 313(3), 145–198. <https://doi.org/10.2475/03.2013.01>
- Guenther, W. R., Reiners, P. W., & Tian, Y. (2014). Interpreting date–eU correlations in zircon (U-Th)/He datasets: A case study from the Longmen Shan, China. *Earth and Planetary Science Letters*, 403, 328–339. <https://doi.org/10.1016/j.epsl.2014.06.050>
- Hames, W. E., & Bowring, S. A. (1994). An empirical evaluation of the argon diffusion geometry in muscovite. *Earth and Planetary Science Letters*, 124(1–4), 161–169. [https://doi.org/10.1016/0012-821X\(94\)00079-4](https://doi.org/10.1016/0012-821X(94)00079-4)
- Heim, A., & Gansser, A. (1939). *Central Himalayas—Geological observations of Swiss expedition, 1936*. *Mem. Soc. Helv. Sci. Nat.*, (Vol. 73, pp. 1–245). Zürich: Gebrüder Fretz.
- Herman, F., Copeland, P., Avouac, J. P., Bollinger, L., Mahéo, G., le Fort, P., et al. (2010). Exhumation, crustal deformation, and thermal structure of the Nepal Himalaya derived from the inversion of thermochronological and thermobarometric data and modeling of the topography. *Journal of Geophysical Research*, 115, B06407. <https://doi.org/10.1029/2008JB006126>
- Hollister, L. S., & Grujic, D. (2006). Pulsed channel flow in Bhutan. In R. D. Law, M. P. Searle, & L. Godin (Eds.), *Channel flow, ductile extrusion and exhumation in continental collision zones*, (pp. 415–423). London: Geol. Soc. Spec. Publ.
- Horton, B. K. (1999). Erosional controls on the geometry and kinematics of thrust belt development in the central Andes. *Tectonics*, 18(6), 1292–1304. <https://doi.org/10.1029/1999TC900051>

- Huerta, A. D., & Rodgers, D. W. (2006). Constraining rates of thrusting and erosion: Insights from kinematic thermal modeling. *Geology*, 34(7), 541–544. <https://doi.org/10.1130/G22421.1>
- Kellett, D. A., & Grujic, D. (2012). New insight into the South Tibetan detachment system: Not a single progressive deformation. *Tectonics*, 31, TC2007. <https://doi.org/10.1029/2011TC002957>
- Kesari, G. K. (2010). *Geology and mineral resources of Arunachal Pradesh*, *Geol. Surv. India*, (Vol. 30). Guwahati: Misc. Pub.
- Klootwijk, C. T., Gee, J. S., Peirce, J. W., Smith, G. M., & McFadden, P. L. (1992). An early India-Asia contact: Paleomagnetic constraints from Ninetyeast Ridge, ODP Leg 121. *Geology*, 20(5), 395–398. [https://doi.org/10.1130/0091-7613\(1992\)020<0395:AEIACP>2.3.CO;2](https://doi.org/10.1130/0091-7613(1992)020<0395:AEIACP>2.3.CO;2)
- Kohn, M. J., Paul, S. K., & Corrie, S. L. (2010). The lower Lesser Himalayan sequence: A Paleoproterozoic arc on the northern margin of the Indian plate. *Geological Society of America Bulletin*, 122(3-4), 323–335. <https://doi.org/10.1130/B26587.1>
- Koons, P. O. (1989). The topographic evolution of collisional mountain belts: A numerical look at the Southern Alps, New Zealand. *American Journal of Science*, 289, 1041–1069.
- Landry, K. R., Coutand, I., Whipp, D. M. Jr., Grujic, D., & Hourigan, J. K. (2016). Late Neogene tectonically driven crustal exhumation of the Sikkim Himalaya: Insights from inversion of multithermochronologic data. *Tectonics*, 35, 833–859. <https://doi.org/10.1002/2015TC004102>
- Law, R. D., Jessup, M. J., Searle, M. P., Francis, M. K., Waters, D. J., & Cottle, J. M. (2011). Telescoping of isotherms beneath the South Tibetan Detachment System, Mount Everest Massif. *Journal of Structural Geology*, 33(11), 1569–1594. <https://doi.org/10.1016/j.jsg.2011.09.004>
- Lock, J., & Willett, S. (2008). Low-temperature thermochronometric ages in fold-and-thrust belts. *Tectonophysics*, 456(3-4), 147–162. <https://doi.org/10.1016/j.tecto.2008.03.007>
- Long, S., & McQuarrie, N. (2010). Placing limits on channel flow: Insights from the Bhutan Himalaya. *Earth and Planetary Science Letters*, 290(3-4), 375–390. <https://doi.org/10.1016/j.epsl.2009.12.033>
- Long, S., McQuarrie, N., Tobgay, T., Coutand, I., Cooper, F. J., Reiners, P. W., et al. (2012). Variable shortening rates in the eastern Himalayan thrust belt, Bhutan: Insights from multiple thermochronologic and geochronologic data sets tied to kinematic reconstructions. *Tectonics*, 31, TC5004. <https://doi.org/10.1029/2012TC003155>
- Long, S., McQuarrie, N., Tobgay, T., & Grujic, D. (2011). Geometry and crustal shortening of the Himalayan fold-thrust belt, eastern and central Bhutan. *Geological Society of America Bulletin*, 123(7-8), 1427–1447. <https://doi.org/10.1130/B30203.1>
- Long, S., McQuarrie, N., Tobgay, T., & Hawthorne, J. (2011). Quantifying internal strain and deformation temperature in the eastern Himalaya, Bhutan: Implications for the evolution of strain in thrust sheets. *Journal of Structural Geology*, 33(4), 579–608. <https://doi.org/10.1016/j.jsg.2010.12.011>
- Long, S., McQuarrie, N., Tobgay, T., Rose, C., Gehrels, G., & Grujic, D. (2011). Tectonostratigraphy of the Lesser Himalaya of Bhutan: Implications for the along-strike stratigraphic continuity of the northern Indian margin. *Geological Society of America Bulletin*, 123(7-8), 1406–1426. <https://doi.org/10.1130/B30202.1>
- Long, S. P., Gordon, S. M., & Soignard, E. (2017). Distributed north-vergent shear and flattening through Greater and Tethyan Himalayan rocks: Insights from metamorphic and strain data from the Dang Chu region, central Bhutan. *Lithosphere*, 9(5), 774–795. <https://doi.org/10.1130/L655.1>
- Long, S. P., Gordon, S. M., Young, J. P., & Soignard, E. (2016). Temperature and strain gradients through Lesser Himalayan rocks and across the Main Central thrust, south-central Bhutan: Implications for transport-parallel stretching and inverted metamorphism. *Tectonics*, 35, 1863–1891. <https://doi.org/10.1002/2016TC004242>
- Long, S. P., McQuarrie, N., Tobgay, T., Grujic, D., & Hollister, L. (2011). Geologic map of Bhutan. *The Journal of Maps*, 184–192. <https://doi.org/10.4113/jom.2011.1159>
- Mattauer, M. (1986). Intracontinental subduction, crust-mantle décollement and crustal-stacking wedge in the Himalayas and other collision belts. In M. P. Coward, & A. C. Ries (Eds.), *Collision tectonics*, *Geol. Soc. Spec. Publ.*, (Vol. 19, pp. 37–50). <https://doi.org/10.1144/GSL.SP.1986.019.01.02>
- McQuarrie, N., & Ehlers, T. A. (2015). Influence of thrust belt geometry and shortening rate on thermochronometer cooling ages: Insights from thermokinematic and erosion modeling of the Bhutan Himalaya. *Tectonics*, 34, 1055–1079. <https://doi.org/10.1002/2014TC003783>
- McQuarrie, N., & Ehlers, T. A. (2017). Techniques for understanding fold-thrust belt kinematics and thermal evolution. In R. D. Law, J. R. Thigpen, A. J. Merschat, & H. H. Stowell (Eds.), *Linkages and feedbacks in orogenic systems*, *GSA Memoirs*, (Vol. 213, pp. 25–54). [https://doi.org/10.1130/2017.1213\(02\)](https://doi.org/10.1130/2017.1213(02))
- McQuarrie, N., Long, S. P., Tobgay, T., Nesbit, J. N., Gehrels, G., & Ducea M. (2013). Documenting basin scale, geometry and provenance through detrital geochemical data: Lessons from the Neoproterozoic to Ordovician Lesser, Greater, and Tethyan Himalayan strata of Bhutan. *Gondwana Research*, 23(4), 1491–1510. <https://doi.org/10.1016/j.gr.2012.09.002>
- McQuarrie, N., Tobgay, T., Long, S. P., Reiners, P. W., & Cosca, M. A. (2014). Variable exhumation rates and variable displacement rates: Documenting a recent slowing of Himalayan shortening in western Bhutan. *Earth and Planetary Science Letters*, 386, 161–174. <https://doi.org/10.1016/j.epsl.2013.10.045>
- McQuarrie, N. M., Robinson, D., Long, S. P., Tobgay, T., Grujic, D., Gehrels, G., & Ducea M. (2008). Preliminary stratigraphic and structural architecture of Bhutan: Implications for the along strike architecture of the Himalayan system. *Earth and Planetary Science Letters*, 272(1-2), 105–117. <https://doi.org/10.1016/j.epsl.2008.04.030>
- Mitra, S., Priestley, K., Bhattacharyya, A. K., & Gaur, V. K. (2005). Crustal structure and earthquake focal depths beneath northeastern India and southern Tibet. *Geophysical Journal International*, 160(1), 227–248. <https://doi.org/10.1111/j.1365-246X.2004.02470.x>
- Morgan, L. E. (2019). *Argon geochronology data for eastern Bhutan: U.S. Geological Survey data release*. <https://doi.org/10.5066/P9CLDHOQ>
- Mottram, C. M., Warren, C. J., Halton, A. M., Kelley, S. P., & Harris, N. B. W. (2015). Argon behaviour in an inverted Barrovian sequence, Sikkim Himalaya: The consequences of temperature and timescale on ⁴⁰Ar/³⁹Ar mica geochronology. *Lithos*, 238, 37–51. <https://doi.org/10.1016/j.lithos.2015.08.01>
- Najman, Y., Appel, E., Boudagher-Fadel, M., Bown, P., Carter, A., Garzanti, E., et al. (2010). Timing of India–Asia collision: Geological, biostratigraphic and palaeomagnetic constraints. *Journal of Geophysical Research*, 115, B12416. <https://doi.org/10.1029/2010JB007673>
- Ni, J., & Barazangi, M. (1984). Seismotectonics of the Himalayan collision zone: Geometry of the under-thrusting Indian plate beneath the Himalaya. *Journal of Geophysical Research*, 89(B2), 1147–1163. <https://doi.org/10.1029/JB089iB02p01147>
- Orme, D. A., Carrapa, B., & Kapp, P. (2016). Sedimentology, provenance and geochronology of the upper Cretaceous–lower Eocene western Xigaze forearc basin, southern Tibet. *Basin Research*, 27(4), 387–411. <https://doi.org/10.1111/bre.12080>
- Patriat, P., & Achaache, J. (1984). Indian-Eurasian collision chronology has implications for crustal shortening and driving mechanisms of plates. *Nature*, 311(5987), 615–621. <https://doi.org/10.1038/311615a0>

- Powell, C. M., & Conaghan, P. J. (1973). Plate tectonics and the Himalayas. *Earth and Planetary Science Letters*, *20*(1), 1–12. [https://doi.org/10.1016/0012-821X\(73\)90134-9](https://doi.org/10.1016/0012-821X(73)90134-9)
- Rahn, M. K., & Grasemann, B. (1999). Fission track and numerical thermal modeling of differential exhumation of the Glarus thrust plane (Switzerland). *Earth and Planetary Science Letters*, *169*(3–4), 245–259. [https://doi.org/10.1016/S0012-821X\(99\)00078-3](https://doi.org/10.1016/S0012-821X(99)00078-3)
- Rak, A. J., McQuarrie, N., & Ehlers, T. A. (2017). Kinematics, exhumation, and sedimentation of the north central Andes (Bolivia): An integrated thermochronometer and thermokinematic modeling approach. *Tectonics*, *36*, 2524–2554. <https://doi.org/10.1002/2016TC004440>
- Reiners, P. W., Spell, T. L., Nicolescu, S., & Zanetti, K. A. (2004). Zircon (U-Th)/He thermochronometry: He diffusion and comparisons with $^{40}\text{Ar}/^{39}\text{Ar}$ dating. *Geochimica et Cosmochimica Acta*, *68*(8), 1857–1887. <https://doi.org/10.1016/j.gca.2003.10.021>
- Robbins, G. A. (1972). Radiogenic argon diffusion in muscovite under hydrothermal conditions, M.Sc. thesis, Brown Univ., Providence, R. I.
- Robert, X., van der Beek, P., Braun, J., Perry, C., & Mugnier, J.-L. (2011). Control of detachment geometry on lateral variations in exhumation rates in the Himalaya: Insights from low-temperature thermochronology and numerical modeling. *Journal of Geophysical Research*, *116*, B05202. <https://doi.org/10.1029/2010JB007893>
- Schelling, D. (1992). The tectonostratigraphy and structure of the eastern Nepal Himalaya. *Tectonics*, *11*(5), 925–943. <https://doi.org/10.1029/92TC00213>
- Schelling, D., & Arita, K. (1991). Thrust tectonics, crustal shortening, and the structure of the far-eastern Nepal Himalaya. *Tectonics*, *10*(5), 851–862. <https://doi.org/10.1029/91TC01011>
- Shi, Y., & Wang, C. (1987). Two-dimensional modeling of the P - T - t paths of regional metamorphism in simple overthrust terrains. *Geology*, *15*(11), 1048–1051. [https://doi.org/10.1130/0091-7613\(1987\)15%3C1048:TMOTPP%3E2.0.CO;2](https://doi.org/10.1130/0091-7613(1987)15%3C1048:TMOTPP%3E2.0.CO;2)
- Singer, J., Kissling, E., Diehl, T., & Hetényi, G. (2017). The underthrusting Indian crust and its role in collision dynamics of the Eastern Himalaya in Bhutan: Insights from receiver function imaging. *Journal of Geophysical Research: Solid Earth*, *122*, 1152–1178. <https://doi.org/10.1002/2016JB013337>
- Stüwe, K., & Foster, D. (2001). $^{40}\text{Ar}/^{39}\text{Ar}$, pressure, temperature and fission track constraints on the age and nature of metamorphism around the Main Central Thrust in the eastern Bhutan Himalaya. *Journal of Asian Earth Sciences*, *19*(1–2), 85–95. [https://doi.org/10.1016/S1367-9120\(00\)00018-3](https://doi.org/10.1016/S1367-9120(00)00018-3)
- Thiede, R. C., & Ehlers, T. A. (2013). Large spatial and temporal variations in Himalayan denudation. *Earth and Planetary Science Letters*, *371*–*372*, 278–293.
- Warren, C. J., Singh, A. K., Roberts, N. M. W., Regis, D., Halton, A. M., & Singh, R. B. (2014). Timing and conditions of peak metamorphism and cooling across the Zimthang Thrust, Arunachal Pradesh, India. *Lithos*, *200*, 94–110.
- Webb, A. A. G. (2013). Preliminary balanced palinspastic reconstruction of Cenozoic deformation across the Himachal Himalaya (northwestern India). *Geosphere*, *9*(3), 572–587. <https://doi.org/10.1130/GES00787.1>
- Webb, A. A. G., Yin, A., Harrison, T. M., Célérier, J., Gehrels, G. E., Manning, C. E., & Grove, M. (2011). Cenozoic tectonic history of the Himachal Himalaya (northwestern India) and its constraints on the formation mechanism of the Himalayan orogen. *Geosphere*, *7*(4), 1013–1061. <https://doi.org/10.1130/GES00627.1>
- Whipp, D. M. Jr., Ehlers, T. A., Braun, J., & Spath, C. D. (2009). Effects of exhumation kinematics and topographic evolution on detrital thermochronometer data. *Journal of Geophysical Research*, *114*, F04021. <https://doi.org/10.1029/2008JF001195>
- Whipple, K. (2014). Can erosion drive tectonics? *Science*, *346*(6212), 918–919. <https://doi.org/10.1126/science.aaa0887>
- Whipple, K. X. (2009). The influence of climate on the tectonic evolution of mountain belts. *Nature Geoscience*, *2*(2), 97–104. <https://doi.org/10.1038/ngeo413>
- Willett, S. D. (1999). Orogeny and orography: The effects of erosion on the structure of mountain belts. *Journal of Geophysical Research*, *104*(B12), 28957–28981. <https://doi.org/10.1029/1999JB900248>
- Willett, S. D., & Brandon, M. T. (2002). On steady states in mountain belts. *Geology*, *30*(2), 175–178. [https://doi.org/10.1130/0091-7613\(2002\)030<0175:OSSIMB>2.0.CO;2](https://doi.org/10.1130/0091-7613(2002)030<0175:OSSIMB>2.0.CO;2)
- Wobus, C. W., Hodges, K. V., & Whipple, K. X. (2003). Has focused denudation sustained active thrusting at the Himalayan topographic front? *Geology*, *31*(10), 861–864. <https://doi.org/10.1130/G19730.1>
- Wobus, C. W., Whipple, K. X., & Hodges, K. V. (2006). Neotectonics of the central Nepalese Himalaya: Constraints from geomorphology, detrital $^{40}\text{Ar}/^{39}\text{Ar}$ thermochronology, and thermal modeling. *Tectonics*, *25*, TC4011. <https://doi.org/10.1029/2005TC001935>
- Woodward, N. B., Boyer, S. E., & Suppe, J. (1989). *Balanced geological cross-sections: An essential technique in geological research and exploration, Short Course Geol.*, (Vol. 6). Washington, D. C: American Geophysical Union.
- Yin, A. (2006). Cenozoic tectonic evolution of the Himalayan orogen as constrained by along-strike variation of structural geometry, exhumation history, and foreland sedimentation. *Earth-Science Reviews*, *76*(1–2), 1–131. <https://doi.org/10.1016/j.earscirev.2005.05.004>
- Yin, A., Dubey, C. S., Kelty, T. K., Webb, A. A. G., Harrison, T. M., Chou, C. Y., & Célérier, J. (2010). Geological correlation of the Himalayan orogen and Indian craton: Part 2—Structural geology, geochronology, and tectonic evolution of the eastern Himalaya. *Geological Society of America Bulletin*, *122*(3–4), 360–395. <https://doi.org/10.1130/B26461.1>